universität wien

MASTERARBEIT / MASTER'S THESIS

Titel der Masterarbeit / Title of the Master's Thesis

„Matter-wave interferometry with improved biomolecular sources“

verfasst von / submitted by

Philipp Rieser, BSc

angestrebter akademischer Grad / in partial fulfillment of the requirements for the degree of

Master of Science (MSc)

Wien, 2019 / Vienna, 2019

Studienkennzahl lt. Studienblatt / degree programme code as it appears on the student record sheet:	A 066 876
Studienrichtung lt. Studienblatt / degree programme as it appears on the student record sheet:	Masterstudium Physik
Betreut von / Supervisor:	Univ. Prof. Dr. Markus Arndt

Abstract

Quantum interference experiments are a powerful tool in the probing of the wave nature of matter. Due to their sensitivity to minute perturbations, matter-wave interferometers have a wide range of applications, enabling high precision measurements of natural constants, external forces and the internal properties of materials. Such information is particularly interesting for biomolecules, since their internal properties are of great interest and difficult to access using classical methods. However, they are fragile and difficult to translate into the gas phase. Many source techniques used in atom interferometry to provide a stable intense atom beam, such as evaporative heating and short pulse laser desorption, cannot be translated to massive biomolecules.

In this thesis I present a demonstration of the de Broglie-wave nature of the antibiotic polypeptide Gramicidin, a natural biomolecule with a mass of 1882 amu. This achievement required the improvement of a short pulse laser desorption source for the Optical TIme domain MAtter wave interferometer (OTIMA) to obtain a stable intense beam of neutral, intact and mass selected polypeptides.

The observed interference fringes are compared to a model of the phase space expectation, accounting for effects such as beam tilts and mirror imperfections, to determine their quantum mechanical nature. To this end, a combination of auxiliary measurements and quantum chemical computations determine the relevant optical properties that allow distinction between classical Moiré shadow and quantum phase revival.

The source adaptations are also used to perform molecular beam experiments with masses exceeding 20,000 amu. The molecules in question are tailored to maximize the efficiency of Vacuum UltraViolet (VUV) photoionization. The successful desorption and detection of a neutral molecular beam with such masses has previously been impossible.

Zusammenfassung

Quanten Interferenzexperimente sind nützliche Werkzeuge, um die Welleneigenschaften von Materie zu untersuchen. Wegen ihrer großen Empfindlichkeit gegenüber kleinen Störungen haben Materiewelleninterferometer ein breites Anwendungsgebiet. Sie erlauben hochpräzise Messungen von Naturkonstanten, externen Kräften und den internen Eigenschaften von Materialien. Solche Messungen bieten sich besonders gut für Biomoleküle an, da ihre internen Eigenschaften sowohl sehr interessant als auch oft nur schwer klassisch messbar sind. Biomoleküle sind aber auch fragil, und schwer in die Gasphase zu bewegen. Viele Quellmethoden, die in der Atomphysik Anwendung finden, um ein stabiles, langlebiges Signal zu erhalten, lassen sich nicht unmittelbar auf schwere Biomoleküle anwenden.
In dieser Arbeit präsentiere ich das de Broglie-Wellenverhalten des antibiotischen Polypeptides Gramizidin, ein natürliches Biomolekül mit einer Masse von 1882 amu. Diese Leistung benötigte die Verbesserung der kurz-Puls Laser Desorptionsquelle für das Optical TIme domain MAtter wave interferometer (OTIMA), mit welcher der stabile, intensive Strahl von neutralen, Masse-selektierten Biomolekülen erzeugt werden kann.
Die Interferenzmessungen werden mit einem Modell der Phasenraum Erwartungen verglichen, das auf verschiedene Effekte wie einen Tilt im Molekularstrahl und Mängel am Interferometerspiegel Rücksicht nimmt, um ihre quantenmechanische Natur zu beweisen. Hierfür wurde eine Kombination aus Hilfsmessungen und quantenchemischer Berechnungen verwendet, um die relevanten optischen Eigenschaften zu bestimmen, die es erlauben, zwischen klassischem Moiré Schatten und quantenmechanischer Phasenerneuerung zu unterscheiden.
Die Adaptionen der Quelle werden zusätzlich dazu verwendet, Molekulahrstrahlexperimente mit Massen höher als 20,000 amu auszuführen. Die verwendeten Moleküle sind maßgeschneidert um die Effizienz von Vakuum-Ultravioletter (VUV) Photoionisation zu maximieren. Die erfolgreiche Desorption und Detektion von einem neutralem Molekularstrahl einer solchen Masse war früher unmöglich.

Contents

1 Introduction

In the 20th century our conceptual understanding of the world we live in grew by leaps and bounds. In the realm of the massive, the theory of general relativity [1, 2], going beyond the scope of Newtonian mechanics revolutionized the way we look at space and time itself. At the microscopic scale on the other hand, quantum mechanics [1, 3, 4] offered a new way of looking at light and matter. This new theory defied classical expectations, predicting wave-like behavior [3] of particles and the possibility of populating multiple states at once. While some of these claims may sound far fetched, quantum mechanics has withstood every single test of its validity to date. Beginning with diffraction experiments with electrons [5, 6], followed by demonstration of quantum effects for atoms [7], neutrons [8], massive molecules [9] and more recently positrons [10], the history of quantum mechanics is a story of success. Other experiments, showing indisputable quantum behavior of light with photon antibunching [11], or tests of Bell's inequality [12, 13, 14], cement the status of quantum mechanics as one of the best tested theories in physics.
One of the premier tools of visualizing quantum mechanics are matter-wave interferometers and their sensitivity to external perturbations has many possible applications. They are based on Louis de Broglies postulation of a particle characteristic wavelength λ_{dB}, dependent on the momentum of the particle

$$\lambda_{\mathrm{dB}} = \frac{h}{p}. \tag{1}$$

Matter-wave-interferometers can be used to explore models that aim to consolidate the microscopic world of quantum phenomena with the everyday macroscopic world we live in. The prediction of such models, be they decoherence-related [15] or based on wave-function collapse [16, 17], can be probed impartially with matter-wave-interference experiments. Their sensitivity makes interferometers an attractive tool for other areas of research as well. By introducing controlled perturbations, they can be used to learn about particle internal properties. Here biologically relevant molecules are of particular interest. Their internal and electronic properties govern how they interact with their surroundings. Knowledge of these properties could thus grant insight into the complex language of the biological world. For this, the study of unsolvated molecules free from matrix influences is a field of great interest [18]. Decoupling the particle from a matrix can be achieved by gas phase studies.
This poses another challenge. By their nature biomolecules are fragile and difficult to transfer into the gas phase while remaining intact.

Viable options for charged biomolecular beams have found use in been found in Matrix Assisted Laser Desorption Ionization (MALDI) or electrospray ionization and used in several studies [19, 20]. However, many internal and electronic properties are particularly interesting for neutral particles [21]. Studies with neutral molecular beams have proven crucial in analysing the internal and electronic properties of vitamins [22] and oligopeptides[23].
All this leads to the search for more efficient source mechanisms that allow the study of neutral biomolecular systems in a molecule interferometer [24].

This thesis documents the implementation and characterization of a new source mechanism at the Optical Time Domain MAtterwave (OTIMA) interferometer, aimed towards improving the efficiency to produce the stable signal required for probing biomolecular systems. It is important to quantify what characterizes a good source within the parameters of the experiment. To properly align the interferometer, several parameters have to be fine-tuned simultaneously. Achieving an optimum in all of them requires time and stability for the alignment. The second requirement is high signal intensity. This improves the accuracy of the measurements and allows for shorter measurements and more data. The last factor is source efficiency. For more complex and massive biomolecules the availability is reduced by the more difficult synthetization. Here it becomes vitally important to maximize the fraction of usable molecules exiting the source.
However efficient beams of neutral biomolecules must be complemented by efficient detection. Many of the standard detectors require the molecules to be charged. Photoionization is a typical postionization method. However, most biomolecules require ionization energies > 10 eV, exceeding the photon energy of tabletop vacuum ultraviolet (VUV) lasers [25]. This can be circumvented to some extent by multi-photon ionization at high enough pulse intensities in peptides typically up to 2000 amu [26], however in larger molecules the swift relaxation to non-ionizing states [27, 28] suppresses this option. The most easily ionizable building block of proteins is Tryptophan (Trp), with an ionization energy of 7.87 eV. The abundance of Trp in Gramicidin D and several other peptide antibiotics accounts for their ionization behavior [29]. For molecules beyond 2000 amu [28, 27], if they even incorporate Trp into their structure, the ionization probability diminishes quickly. There are several explanations for this behavior, such as electron recapture [30] if the ionized Trp lies at the heart of the folded protein. One approach to overcome this is tested in this thesis. By maximizing the fraction of Trp in the molecule, the chance for several residues to be exposed to vacuum is increased. This bypasses electron recapture, allowing even massive polypeptides with masses exceeding 20,000 amu to be detected.

In this thesis I present the soft fs-laser desorption of biomolecular probes at intensities a factor of 100,000 larger than traditional MALDI experiments. This desorption method allows the ionization study of poly-peptides 10 times longer than other peptides postionized to date.
Based on the more efficient desorption process and increased signal lifetime, matter-wave interference of the antibiotic polypeptide Gramicidin D was performed.

2 Theory

2.1 Diffraction in the near field

Molecular interferometry is an important tool for exploring the nature of matter-waves. Central to the concept of OTIMA is diffraction. To describe diffraction at an aperture an electromagnetic (EM) plane monochromatic wave $U(\vec{x},t) = E_0(\vec{x})\exp(k_0 z - \omega_0 t)$ with wave-number $k_0 = 2\pi/\lambda$ and frequency $\omega_0 = kc$ serves as a perfect example. For stationary aperture the spatial propagation and diffraction of the wave can be described using the Helmholtz equation (2). It is formally identical to the time-independent Schroedinger equation (3) allowing for a seamless transition to molecular de Broglie wave functions later

$$(\Delta + k_0^2)E(\vec{x}) = 0, \tag{2}$$

$$\left(\Delta + k_{\mathrm{dB}}^2\right)\psi(\vec{x}) = 0. \tag{3}$$

The plane wave travels from its origin $\vec{x}_0$ in z-direction and encounters an aperture with transmission function $S(\xi,\eta)$ in the (x,y)-plane (see figure 1).

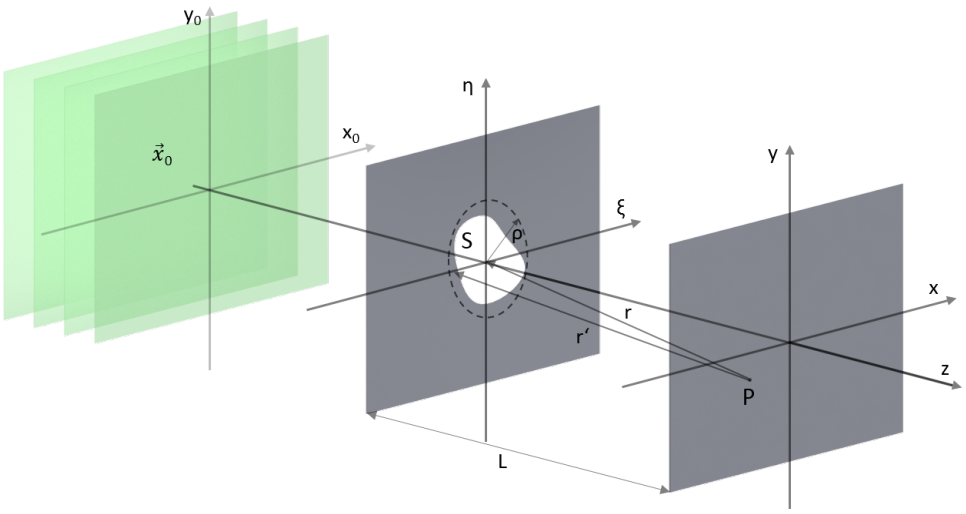

Figure 1: Diffraction of a plane at an aperture S. The relevant area can be approximated with a circle of radius ρ. The final wave function on a screen at a distance L behind the aperture follows from Huygens principle [31]. For a large enough distance L the example propagation paths of length r and r' can be simplified using the paraxial approximation.

According to Huygens principle, the field behind the aperture can be described as a sum of wavelets $E(\xi, \eta)$ originating from the object:

$$E(\vec{x}) = -\frac{i}{\lambda r} \iint_S e^{-ikr} E(\xi, \eta)\ d\xi d\eta. \tag{4}$$

From this point on several assumptions simplify the integral. If the waves are observed from a point $\vec{x}$ where the separation of z and z_0 is much larger than the other spatial separations, one can apply the paraxial approximation along the propagation axis to obtain $r \approx z$.
Additionally, applying the Fresnel approximation to the exponent via 2nd-order Taylor-expansion, we can and find the Fresnel-integral:

$$E(\vec{x}) = -\frac{i}{\lambda z} \iint_S \exp\left(-ik\left[\frac{-x\xi - y\eta}{z} + \frac{\xi^2 + \eta^2}{2z}\right]\right) E(\xi, \eta)\ d\xi d\eta. \tag{5}$$

For most cases, it can only be solved numerically. Looking at the exponent we see two distinct terms: a quadratic term, describing the curvature of the wavefronts, and a linear term. At large distances behind the aperture it is reasonable to ignore the wavefront curvature, retaining only linear terms in the Fraunhofer or far field regime. Closer to the aperture, the curvature cannot be ignored. This is known as the Fresnel or near field regime.
This is the case for distances $L < \rho^2/\lambda$ where ρ^2 is a measure of the area of the aperture.
In the near field regime one may encounter the Talbot effect [32]: If a periodic structure, such as a grating, is illuminated by a monochromatic plane wave, a self-image of that structure is (re)produced at a certain distance behind it. This characteristic distance, the Talbot length L_T depends on the period of the structure d and the wavelength of the illuminating light λ.

$$L_T = \frac{d^2}{\lambda}. \tag{6}$$

Uneven multiples of this distance cause a phase shift in the self-image of half a grating period while even multiples are not shifted[1]. For fractional distances
$L = q/p\ L_\mathrm{T};\ q, p \in \mathbb{N}$ of L_T self-images form with fractional grating period. All of these periodic structures can be summed into a 2D pattern, known as the Talbot carpet, shown in figure 2.

[1] This is why the Talbot distance is sometimes defined as $L_T = \frac{2d^2}{\lambda}$

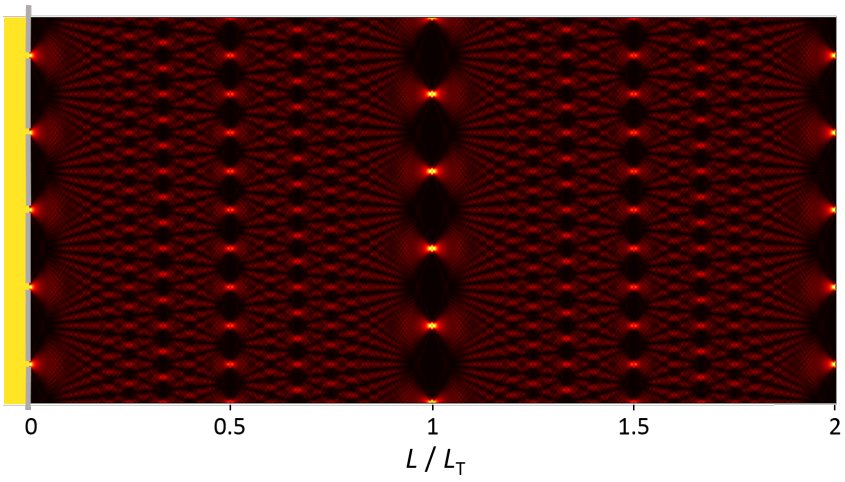

Figure 2: Simulated Talbot Carpet for a monochromatic plane wave. The Visibility of the self-images are dependent on the opening fraction of the grating.

Such a carpet can be obtained from a numerical simulation the wave function behind a one-dimensional grating that was illuminated by a plane wave. The initial Fresnel integral reads

$$E(x,z) = \sqrt{\frac{1}{i\lambda z}} \int_{-\infty}^{\infty} d\xi e^{\frac{i\pi}{\lambda z}(\xi - x)^2} T(\xi). \tag{7}$$

After expanding the transmission into a Fourier series and simplifying the integral by adding a quadratic complement to the exponent, we obtain a numerical estimation

$$E(x,z) = \sum_{l=-N}^{N} T_l \; e^{-\frac{i\pi z}{d^2} l^2} e^{l\frac{2i\pi}{d} x} \tag{8}$$

For the simulation in figure 2, a value of $N = 20$ was chosen. The coefficients T_l are from the Fourier expansion of the single slit transmission function $T(x)$ which is rectangular

$$T_l = \frac{\sin(\pi a l)}{\pi l}, \tag{9}$$

$$T_0 = a. \tag{10}$$

Here, a denotes the opening fraction of the grating $a = s/d$. To observe this effect the incident light must be coherent, both transversally and longitudinally.

The longitudinal coherence L_C

$$L_C \simeq \frac{\lambda^2}{\Delta\lambda} \tag{11}$$

grows with the spectral purity of the source, which is assumed to be monochromatic for figure 2. Spatial coherence is s infinite for plane waves, as assumed in 2. In the more realistic case of an extended source with no internal phase correlation, transversal coherence depends on the distance to the source L and the effective source size s.

$$X_C = \frac{2L\lambda}{s}. \tag{12}$$

Observing such self-images for spatially incoherent sources is possible using an additional grating, placed in front of the first one. This can be seen in figure 3. The second grating is effectively illuminated by a series of point sources, each coherent over several grating orders and producing its own self-image. This effect is known as the Lau effect [33]. The overlapping self-images form the Talbot-Lau carpet behind the second grating. The intensity modulation can then be displayed on a screen. For these self-images to overlap resonantly, the gratings and screen must be placed at certain distances from one another. The most commonly used spacing configuration is $L_1 = L_2 = {L_T}^{(2)}$.
These near field effects can also be applied to matter-waves in near field matter-wave interferometers. They have several advantages over their far field counterparts. The application of the Talbot-Lau effect allows the use of real-world, spatially incoherent sources. Since coherent particle sources usually have low intensity, a Talbot-Lau interferometer (TLI) can work with a comparatively higher particle flux.
An additional advantage is the mass scaling of TLIs. For a fixed interferometer length, the grating period required for high contrast interference scales with the square root of the mass: $d \propto \sqrt{\lambda_{dB}} \propto 1/\sqrt{m}$. This ia a large advantage over the linearly scaling far field requirements and allows the interference of massive particles in a much more compact setting. A symmetric and homogeneous TLI consists of three identical gratings G_1 - G_3 separated symmetrically by a multiple of the Talbot distance. Particle-grating interactions reduce the optimal spacing slightly. The first and second gratings prepare the Talbot-Lau carpet, while the third grating serves as a mask to spatially resolve the interference fringes. Shifting G_3 along the grating vector allows 'scanning' of the interference fringes. A different approach, scanning along the propagation direction z, is done in our experiments below.

[2]This configuration also causes the $\frac{\pi}{2}$-fringe shift at uneven integers of L_T to vanish

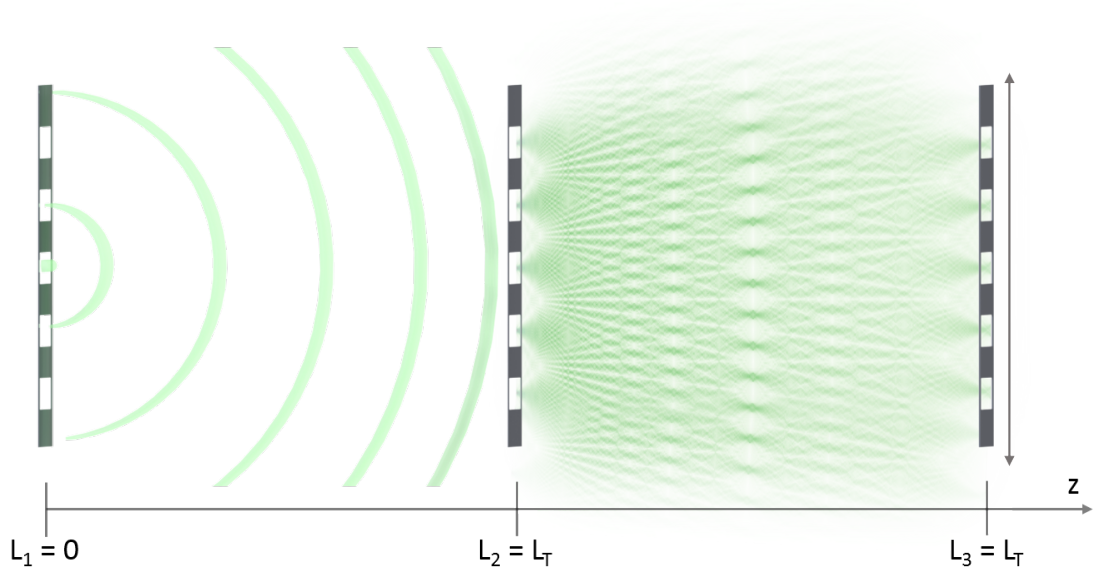

Figure 3: Depiction of the Talbot-Lau interferometer principle. The first grating serves as a mask to produce individual point sources. Light passing through these sources then has sufficient spatial coherence to produce individual (magnified) self-images behind the second grating. A third grating can be used to spatially resolve the intensity modulation of the overlapping Talbot-Lau images by scanning over the intensity modulation.

For a given grating period and separation, high-mass interference is only possible if we reduce the velocity of the molecules. This increases the interaction time of a molecule with the grating and introduces a dispersive phase via molecule-grating interactions caused by the van der Waals and Casimir-Polder potentials [34, 35]. These potentials cause an additional phase shift dependent on the distance of a molecule to the grating wall. This phase shift leads to a position dependent diffraction behind the second grating. For large molecules or long interaction times this can smear out the interference pattern.

2.2 Optical beam splitters

In our present experiment, we use optical gratings created by standing light waves [36]. Optical gratings have seen ample use in matter-wave interferometry [37, 38]. The Kapitza Dirac effect [39], creating a pondermotive potential, can be used to diffract electrons at a standing light wave [40]. Light pulses can be used to speak to the internal states of atoms, taking advantage of Rabi oscillations two switch them between excited and ground states [41].
This principle, using light to speak to the internal state, can also be applied to molecules, overcoming the challenge of dispersive molecule-grating interactions. Such gratings have two particularly interesting and universal ways to interact with molecules: direct absorption of one or more photons or the induction of a dipole moment that interacts with the electric field of the standing wave. The interaction with the electric field adds a phase to the molecules, while direct absorption imparts a momentum change $\pm\hbar k$ onto the molecule, adding a further phase modulation, as long as the molecule is not removed from the beam and as long as it does not re-emit the photon. For sufficient photon energy, an absorbed photon also depletes the molecular beam via ionization or fragmentation. Dipole force gratings have seen application in both far [36] and near field experiments [42].
An all optical interferometer can cope with complex materials as it does not clog or deform upon impact of the particles [43, 44]. The main requirement for an all optical Talbot-Lau interferometer is to have at least two absorptive gratings, if the initial source is spatially incoherent. Transverse coherence [38] is hard to achieve for molecules. Photo depletion allows the first and last grating to prepare spatial coherence and to resolve the interference pattern respectively [45], in a way analogous to material gratings. To achieve maximal contrast, a single absorbed photon shall suffice to a deplete the particle beam. This can be achieved in a variety of ways. Single atoms for instance can be resonantly pumped into a dark state making them undetectable. However, different types of atoms need lasers with different wavelengths which in turn changes L_{T}. With larger particles the multitude of potential relaxation channels poses another problem, since many of them leave the particle in the beam and detected. In a universal interferometer, the photon energy of the gratings must be high enough to cause beam depletion with a single absorption event in many different particles [46]. This requirement allows a process that modulates the beam intensity with respect to the detection [46].

2.3 OTIMA

In OTIMA this is realized with the use of vacuum-ultra-violet (VUV) laser beams retro-reflected from a single CaF mirror. The photon energy of these lasers is higher than the ionization energy of many polyatomic molecules [47] and allows experiments with many biomolecules incorporating the amino acid Tryptophan. The standing light waves with wavelength λ_{L} created by these lasers have a grating period of $d = \lambda_{\mathrm{L}}/2$. All three gratings act both as absorptive masks and as phase gratings. However, at G_1 the particles are not yet sensitive to phase contributions, due to their own random phase coming from an incoherent source. In a similar vein, G_3 as the last grating serves the purpose of resolving the intensity modulation of the molecular beam. Only G_2 imprints a relevant phase on the passing molecules, while G_1 and G_3 act as absorptive masks.
The opening fraction of the gratings can be tuned by changing the laser power. High pulse energy translates to an increased absorption probability even close to the nodes. The pulsed nature of the grating lasers leads to another aspect of OTIMA: it operates in the time-domain. By activating the laser gratings in three sharp time intervals, close to the so-called Talbot-time T_{T}, the particles see a Talbot Lau interferometer. The Talbot time is a measure of the time between quantum phase revivals of the grating function

$$T_{\mathrm{T}} = \frac{L_{\mathrm{T}}}{v} = \frac{d^2 m}{h}. \tag{13}$$

A depiction of this arrangement is shown in figure 4. This phenomenon can also be seen from another viewpoint. In a semiclassical treatment, the particles localized at the grating openings receive a momentum uncertainty parallel to the grating vector, with its strength inversely proportional to the size of the grating opening. This causes a superposition of recoils parallel and anti-parallel to the grating but leaves the forward momentum unchanged. Therefore it is the flight time between two gratings and not their spatial separation that plays the crucial role in the wave evolution.
From eq. (13) one can see that in the time-domain the optimal grating separation is velocity independent. In addition, many phase averaging effects caused by a finite velocity distribution are removed because all molecules experience the same evolution time between the gratings, independent of their velocity.

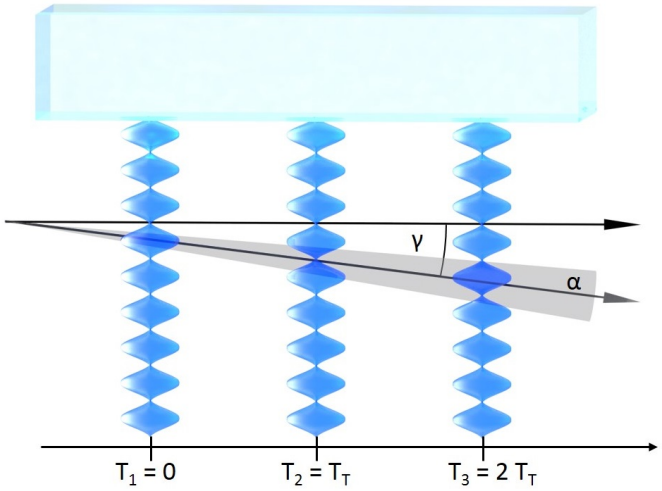

Figure 4: Depiction of the OTIMA interferometer mirror. Three VUV laser beams are retro reflected from a single mirror, producing the absorptive light gratings. Particles passing through the antinodes of the standing waves are expelled from the molecular beam, either being fragmented or ionized. Passing through the nodes, however, leaves the particles intact. The pulsed lasers illuminate the particles with a temporal separation of the Talbot time T_{T}. The tilt of the molecular beam with regards to the mirror surface is denoted with γ. The divergence of the beam is given by α.

Phase averaging due to the Coriolis force remains [48], but is negligible for up to large masses [49]. This robustness to velocity dephasing at a price. There needs to be a velocity class in which the particles interact with every grating, requiring either precise velocity control or wide velocity distributions.
A single mirror for all three gratings makes the setup especially robust to vibrational dephasing [43], canceling out quasi-static tilts and shifts of the mirror.
The pulsed nature of the light gratings opens up several options for source and detection mechanism. Pulsed experiments are compatible with a wide variety of different sources. One example is laser desorption. The technology for pulsing neutral biomolecular beams is currently further advanced than for continuous counterparts. Pulsed desorption and ionization lasers, operating with intensities unrivalled by their continuous wave (CW) equivalents. High intensity is key in obtaining the needed ionization yield to make OTIMA workable. Additionally, VUV lasers have no CW equivalent.

2.4 Molecule propagation through OTIMA

The Talbot Lau principle has been used with light [50] and matter-waves [38, 51]. Its mathematical formalism in the time domain has been described as well [38, 52, 43]. This section will give a brief overview of the mathematical formalism for OTIMA, used for our simulations and predictions. The description is based on several assumptions: Absorption of a single photon is assumed to be sufficient to remove the particle from the beam. The gratings show a periodic modulation only in the x-direction and are invariant (on the scale of the grating period) to translation in the z-y plane. The grating pulses must be short enough to neglect the particle movement during illumination, while being long enough to have a workable longitudinal coherence. The lasers in OTIMA have a $1/e$ coherence length of $L_C = 2.9$ cm, with a pulse duration of 8 ns. The spatial extension of the particles must be much smaller than the grating period to neglect Rayleigh and Mie scattering and for the dipole approximation to be valid. Rayleigh scattering causes significant visibility reduction for particle diameters larger than 20 nm[49]. Mie scattering significantly reduces the transmission of the interferometer for diameters of 13 nm[53]. The tilt of the molecular beam must be small enough to make the movement along the grating vector during interaction with the laser τ small compared to the period $v_\gamma \tau \ll d$ to prevent averaging over several grating periods. With a laser pulse duration of 8 ns, a velocity of $v_\gamma = 10$ m/s would be enough to destroy the interference pattern.
The tilt must also fall within the limits of the paraxial approximation. The transversal and longitudinal quantum state can be separated due to the difference of their respective velocities. This reduces the calculations to a one dimensional modulation along x-axis, the eikonal approximation [54, 55].
An elegant way of formulating the particle-propagation through the interferometer is using Wigner functions $w(x, p)$ [56, 54]. Here, x denotes position and p momentum of the molecular center-of-mass motion. It is defined by the transformation of the density matrix in position space $\rho(x, x') = \langle x|\hat{\rho}|x\rangle$. This takes into account the ensemble of states entering the interferometer and decoherence processes. The advantage of the Wigner formalism is its nature as a quasi-probability distribution. This allows for a semi-classical treatment of the particle trajectories and a simple comparison to a classical phase space density $f(x, p)$

$$w(x,p) = \frac{1}{h}\int ds\ \exp\left(\frac{ips}{\hbar}\right)\langle x + \frac{s}{2}|\hat{\rho}|x + \frac{s}{2}\rangle. \tag{14}$$

With the Wigner function the evolution of the particle state as it passes through the interferometer can be described in a scattering approach: every free evolution is followed by an interaction with a grating.

This repeats for every grating, leading to a set of Wigner functions describing every step of the way. The free evolution of the Wigner function is a shearing transformation

$$w_t(x,p) = w_0\left(x - \frac{pt}{m}, p\right) \tag{15}$$

which is is formally analogous to the evolution of the classical phase space density:

$$f_t(x,p) = f_0\left(x - \frac{pt}{m}, p\right). \tag{16}$$

For a complete description of the free evolution a constant acceleration, due to external forces such as electromagnetic fields or gravity, and a shift $p_\gamma = mv\tan(\gamma)$ caused by a tilt γ of the beam must be accounted for

$$w_t(x,p) = w_0\left(x - \frac{pt}{m} - \frac{p_\gamma t}{m} - \frac{at^2}{2}, p - p_\gamma - amt\right). \tag{17}$$

The interaction with a grating is described by the convolution of the Wigner function with the grating kernel $T^{(\mathrm{k})}(x,p)$ of the k-th grating

$$w'(x,p) = \int dk\; T^{(\mathrm{k})}(x, p-k) w(x,k), \tag{18}$$

$$T^{(\mathrm{k})}(x,p) = \frac{1}{h}\int ds\; \exp\left(\frac{ips}{\hbar}\right) t^{(\mathrm{k})}(x - \frac{s}{2}) t^{(\mathrm{k})*}(x + \frac{s}{2}). \tag{19}$$

The complex transmission function $t(x)$ forming the kernel has two main components

$$t^{(\mathrm{k})}(x) = \exp\left[\left(-\frac{n_0}{2} + i\phi_0\right)\cos^2\left(\frac{\pi x}{d}\right)\right]. \tag{20}$$

The real part of $t(x)$ is a measure for the transmission probability $|t(x)|^2$ of a particle traversing the grating at position x.
In addition to depletion of the molecular beam, the particles traversing the grating also experience a phase shift. This is due to coupling of the dipole polarizability α_L to the light field $E^{(\mathrm{k})}$. This effect leads to the imaginary part of $t(x)$. The parameters $n_0^{(\mathrm{k})}$ and $\phi_0^{(\mathrm{k})}$ are the number of absorbed photons in an antinode and the average phase shift due to polarization respectively

$$n_0^{(\mathrm{k})} = \frac{\sigma_\mathrm{L} E^{(\mathrm{k})} \lambda_\mathrm{L}}{hcA_\mathrm{L}}, \tag{21}$$

$$\phi_0^{(\mathrm{k})} = \frac{4\pi^2 E^{(\mathrm{k})} \alpha_\mathrm{L}}{hcA_\mathrm{L}}. \tag{22}$$

Here σ_{L} denotes the absorption cross-section of the particle and α_{L} its polarizability. The factors $E^{(\mathrm{k})}$, λ_{L} and A_{L} describe the pulse energy, wavelength and illumination area respectively.
For a more realistic treatment of the light gratings [57], additional factors must be considered. A mirror reflectivity $R < 1$ reduces the overall number of photons contributing to the standing light wave. In addition to this, mirror deformations and the limited longitudinal coherence of the grating lasers add an incoherent sum of running waves to the standing light field. To account for these factors, the grating energy $E^{(\mathrm{k})}(x)$ can split into separate terms describing these contributions:

$$E^{(\mathrm{k})}(x) = \left[R(1-C) + (1-R) + 4CR\cos^2\left(\frac{2\pi x}{\lambda \mathrm{L}}\right)\right] E^{(\mathrm{k})}. \tag{23}$$

Here C describes the coherence of the standing light wave $0 < C < 1$. With this modification to $E^{(\mathrm{k})}$ $n_0^{(\mathrm{k})}$ and $\phi_0^{(\mathrm{k})}$ are effectively reduced for determining their contribution to the interference pattern. The reduction factor is the product of mirror reflectivity R and grating coherence C.

$$n_{0,\mathrm{eff}}^{(\mathrm{k})} = RC\ n_0^{(\mathrm{k})}, \tag{24}$$

$$\phi_{0,\mathrm{eff}}^{(\mathrm{k})} = RC\ \phi_0^{(\mathrm{k})}. \tag{25}$$

With a Fourier expansion of (11) one can describe the Transmission kernel in terms of the Talbot-coefficients B_l

$$T^{(\mathrm{k})}(x,p) \ = \ \frac{1}{h}\sum_{l=-\infty}^{\infty} \exp\left(\frac{2\pi i n x}{d}\right) \int ds\ \exp\left(\frac{ips}{h}\right) B_l^{(\mathrm{k})}\left(\frac{s}{d}\right). \tag{26}$$

They in turn are described by Bessel functions of the first kind J_l.

$$\begin{aligned} B_l^{(\mathrm{k})}(\chi) = \exp\left(\frac{-n_0^{(\mathrm{k})}}{2}\right) \left(\frac{\sin(\pi\chi) - \beta\cos(\pi\chi)}{\sin(\pi\chi) + \beta\cos(\pi\chi)}\right)^{\frac{l}{2}} \\ \times J_l\left(\mathrm{sgn}\left(\frac{\sin(\pi\chi)}{\beta} + \cos(\pi\chi)\right) \frac{n_0^{(\mathrm{k})}}{2\beta}\sqrt{\sin^2(\pi\chi) - \beta^2\cos^2(\pi\chi)}\right). \end{aligned} \tag{27}$$

The dimensionless coefficient β is the relative strength of the absorptive effect of the grating versus its phase effect:

$$\beta = \frac{n_0^{(\mathrm{k})}}{\phi_0^{(\mathrm{k})}} = \frac{\sigma_{\mathrm{L}}\lambda_{\mathrm{L}}}{8\pi^2\alpha_{\mathrm{L}}}. \tag{28}$$

Typical values of β fall between between 0.4 and 0.7 [57]. The classical counterparts to the Talbot coefficients $C_n^{(\mathrm{k})}$ can be obtained by taking the limit of small $\chi = lT/T_\mathrm{T}$: $\sin(\pi\chi) \to \pi\chi$, $\cos(\pi\chi) \to 1$.
For the beam propagation through the interferometer the initial beam is considered to be incoherent with a spatial extension $X_0 \gg d$ and a transverse momentum distribution $D(p_x + p_\gamma)$. Here p_γ denotes an additional constant shift due to a tilt in the molecular beam. The initial Wigner function has the following form

$$w_0(x, p_x) = \frac{1}{X_0} D(p_x + p_\gamma). \tag{29}$$

After following the evolution of the Wigner function through the interferometer and taking its marginal (integral over P) to retrieve the position distribution, one arrives at the detected signal $S(\Delta x, T, \tau)$ behind the last grating. Here its important to consider the Fourier transform $\tilde{D}(x)$ of the momentum distribution

$$\tilde{D}(x) = \int dp \exp\left(\frac{-ips}{\hbar}\right) D(p). \tag{30}$$

Due to the large initial momentum distribution $\tilde{D}$ is a very narrow function, limiting the choice of timings T_1 and T_2. One viable choice is a near-symmetric configuration $T_1 = T_\mathrm{T}$, $T_2 = T_\mathrm{T} + \tau$, with a pulse delay $|\tau| \ll T_\mathrm{T}$.
The end result is the detected signal $S(\Delta x_s, T, \tau)$ after the last grating

$$S(\Delta x, T, \tau) = \sum_l S_l \exp\left[\frac{2\pi i l}{d} \Delta x\right], \tag{31}$$

$$S_l = \tilde{D}\left(\frac{l\tau}{T_T} d\right) B_{-l}^{(1)}(0) B_{2l}^{(2)}\left(\frac{l(T+\tau)}{T_T}\right) B_{-l}^{(3)}(0). \tag{32}$$

Here Δx is the total fringe shift due to mirror deformations Δx_s, external accelerations such as gravity and a tilt of the molecular beam

$$\Delta x = \Delta x_s - \frac{p_\gamma \tau}{m} - aT^2 - 2a\tau T - a\frac{\tau^2}{2}. \tag{33}$$

The periodic modulation of S can be scanned by either changing the grating displacement Δx or introducing a variable delay τ_int to the timing of a grating pulse. During this time the velocity component v_γ causes the particles to travel along the grating vector. Scanning over τ_int shows a sinusoidal modulation enveloped by a Gaussian distribution [58].

2.5 Discrimination of quantum and classical effects

An additional quantity that is useful to verify quantum behavior is the overall amplitude of the signal modulation. For a perfect sine wave it is commonly given by the visibility $\mathcal{V}$:

$$\mathcal{V} = \frac{S_{\max} - S_{\min}}{S_{\max} + S_{\min}} \tag{34}$$

This measure for the fringe amplitude is extracted by observing the maxima and minima of the spatial fringe oscillation. However, in the OTIMA setup scanning the spatial profile of the molecular beam is challenging. Here, the normalized signal difference S_N is a more applicable measure of the amplitude modulation

$$S_{\mathrm{N}} = \frac{S_{\mathrm{int}} - S_{\mathrm{ref}}}{S_{\mathrm{ref}}}. \tag{35}$$

S_{int} is the signal measured from a symmetric measurement at equal grating delays $T_2 - T_1 = T_3 - T_2$. To measure the reference signal S_{ref} the third grating pulse is delayed slightly which causes the fringe modulation to vanish, as seen in fig 5.
The tilt in the molecular beam thus allows indirect scanning of the spatial fringes. This is achieved by introducing a variable delay τ_{int} to the symmetric measurement. During this time, the molecules travel with the transverse velocity v_γ along the grating vector. This way different delays correspond to a different spatial position of the intensity distribution. Simulations showing the impact of the choice of τ_{ref} on such measurements are presented in figure 5:

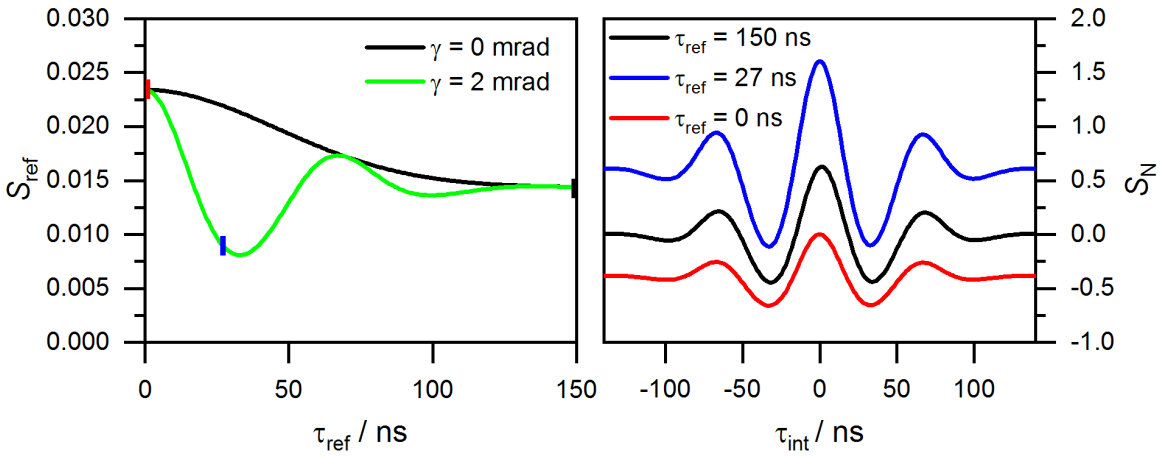

Figure 5: Simulation of the observed fringe modulations for different pulse delays. The reference mode is delayed by τ_{ref}. In the optimal case this causes a loss of fringe modulation but leaves the transmission of the gratings unchanged. For a dip measurement the symmetric mode is also detuned by a varying τ_{int} to scan over the resonance of the interferometer. The choice of τ_{ref} can lead to over (blue) or underestimated (red) contrast.

The detuning time for the reference should be chosen with care. If the detuned measurement still falls within the coherent envelope, the resulting contrast determined from 35 can be an over- or underestimation of the actual contrast. Choosing a detuning that is too large could allow the particle to travel out of the light grating. This would make the reference useless.
From the observed contrast S_{N} one can discriminate between a classical shadow and a quantum phase revival. This is achieved by feeding relevant parameters from the experiment into a simulation based on eq. (32) to obtain the expected contrast. The parameter β plays a crucial role in this. From figure 6 it can be seen that while the quantum expectation is insensitive to β at integer Talbot-orders, the classical analogue is not. This introduces the possibility of a Moiré shadow mimicking the fringe oscillation to an indistinguishable degree. Therefore, knowledge of β or measurements spanning several Talbot-orders are required to validate the quantum nature of the measured contrast.

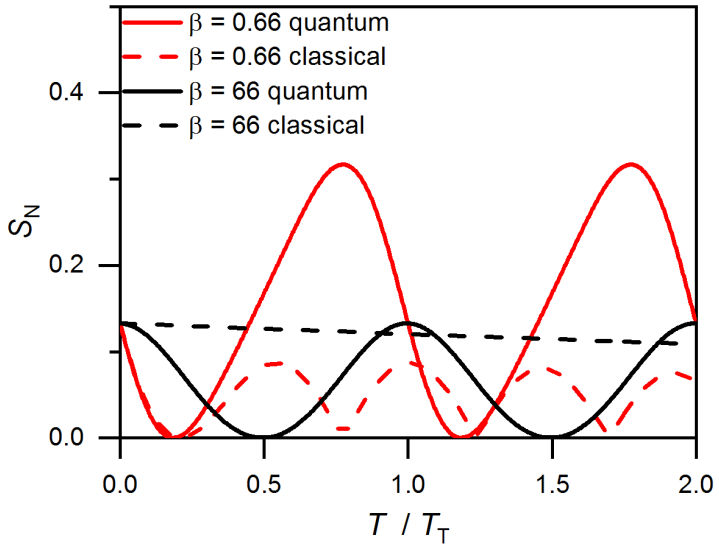

Figure 6: Contrast simulations over several Talbot orders comparing classical and quantum expectations for different values of β. For a value of $\beta = 66$, the classical and quantum expectation are nearly identical at the first Talbot order.

Determining β can be done by combining quantum chemical computations for α_{L} and direct measurement of the absorption cross-section σ_{L}.

2.6 Electronic properties

The quantum nature of the recorded interference fringes described in this thesis is on quantum chemical computation of the dynamic polarizability α_{L} combined with experimental measurement of σ_{L}. This section gives a brief overview of the assumptions and algorithms that are used to estimate this value of β.
The relevant cross-sections in OTIMA are the photoionization cross-section σ_{PI} and the photofragmentation cross-section σ_{PD}, since both contribute to beam modulating effects. For high photon energy, the ionization typically outweighs fragmentation, due to the internal timescales involved. This makes σ_{PI} a strong lower bound for the relevant cross section at OTIMA.
There are several options for obtaining σ_{PI} at λ_{L}. One possibility is to study the ionization yield for varying fluence. Assuming N_0 molecules in each pulse, during illumination by a laser pulse of duration τ and intensity I, the number of ionized

molecules N follows Beer's law:

$$\frac{dN}{N_0 - N} = \sigma_\lambda I \; dt. \tag{36}$$

From this, the number of ionized molecules N can be computed as a function of laser fluance ϕ

$$\int_{N(0)}^{N(\tau)} \frac{dN}{N_0 - N} = \int_0^\tau \sigma_\lambda I \; dt, \tag{37}$$

$$\frac{N_0 - N(\phi)}{N_0} = \exp\left(-\sigma_\lambda \phi\right), \tag{38}$$

$$N(\phi) = N_0 \left(1 - \exp\left(-\sigma_\lambda \phi\right)\right). \tag{39}$$

This relation can then be used to extract σ_λ from a fit to a fluence dependent measurement of the signal intensity.
The polarizability α_{L}, however, cannot easily be estimated at the grating wavelength of 157.5 nm. Instead, we refer to quantum chemical calculations, where molecules are described by their Potential Energy Surface (PES) [59]. The multidimensional PES assigns an electronic energy to every nuclear arrangement within the molecule. It spans the parameter space of all possible conformations of the atoms in normal coordinates, with certain configurations inhabiting local or global minima on the surface. The molecule strives to inhabit the lowest possible energy state on the surface compatible with the stored internal energy. At high temperatures a broad spectrum of configurations can be inhabited. Finding the stable configuration minima requires a tool to scan over the PES. One such method is molecular dynamics (MD) simulations. In such simulations the atoms are allowed to interact with one another over a fixed time period. These interactions are governed by a potential function between the atoms.
A full quantum treatment of this potential requires enormous computing power. To facilitate the computation several approximations are applied: The Born-Oppenheimer approximation [59] treats the electron-nucleus interaction as instantaneous reactions of the electrons to their nuclei, allowing them to be treated as a separate system for every nuclear arrangement. The atomic nuclei themselves are approximated to be point particles following Newtonian mechanics. The electronic state equation has to be solved for a fixed geometry. There are different approaches to solving this equation. Here we use the Density Functional Theory (DFT) [59] method. In DFT, the Schroedinger equation of the electrons is solved by using functionals of the spatially dependent electron density, as opposed to a direct treatment of their wave-functions.

To obtain a value fo α_{L} the following steps were taken. The geometry required for solving the Schroedinger equation of the electrons was calculated by using ab-initio MD. For a given initial geometry a viable configuration on the PES was obtained using a leap frogg algorithm. For this geometry, the Schroedinger equation was solved using DFT, resulting in a theoretical prediction of α_{L}.

3 Experimental setup

3.1 Overview

The OTIMA experiment, depicted in figure 7, extends over several vacuum chambers: the Source Chamber (SC), the Main Chamber (MC) and the Optics Chamber (OC). The SC houses a pulsed laser desorption source, producing a molecular beam that traverses the interferometer.
It connects to the MC via a differential pumping stage. A skimmer with 2 mm aperture diameter separates the two pressure regions.

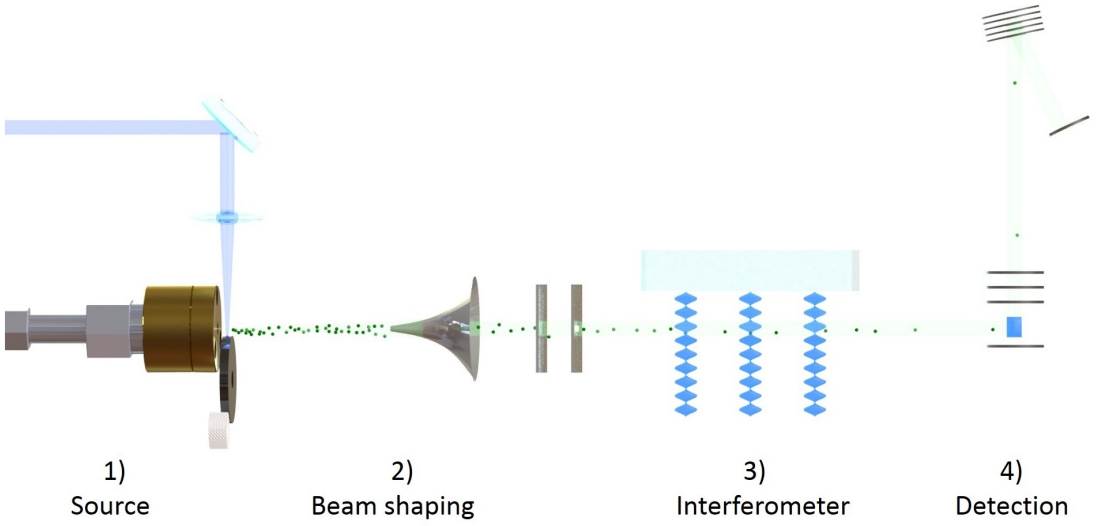

Figure 7: Picture of the OTIMA setup. 1) to 4) details the experimental steps: 1)Source: Particles are desorbed from a glassy carbon wheel using a 343 nm fs laser with a pulse energy of 35 μJ. A supersonic noble gas jet envelops the molecule cloud and carries them toward the interferometer.
2)Beam shaping: Along the way the particle beam (green spheres) is shaped and collimated using a skimmer and delimiters with variable width. 3)Interferometer: The particles pass close to the interferometer mirror and interact with the standing light waves in sequence to form interference fringes. 4)Detection: The surviving particles are ionized by a VUV laser pulse in the repeller region of a reflectron time-of-flight(ToF) mass spectrometer. The particles are accelerated to the drift region and detected at a triple stack of microchannel plates (MCP).

The main chamber houses the interferometer mirror in a movable mount and the Time of Flight(ToF) mass spectrometer . In addition two translation stages connected to horizontal and vertical delimiters allow collimation of the molecular beam as it enters the main chamber. It is pumped by three molecular pumps which prepare a background pressure of 3×10^{-9} mbar. In the main chamber the molecular beam is first collimated. It then passes through the interferometer and is illuminated by three standing light waves formed by F_2-laser beams ($\lambda_L = 157$ nm), retro-reflected from a single VUV dielectric mirror. The three laser beams are guided to the interferometer mirror from the optics chamber bellow. In the OC two motorized mirror stages per laser allow for precise alignment of the light-gratings. After passing through the interferometer the molecules are ionized by a fourth F_2 laser and are subsequently detected with a ToF mass spectrometry (MS).

3.2 Source

OTIMA imposes several requirements on a suitable source. It must be able to produce precise, short, well defined pulses so as not to allow particles to be detected that have not interacted with all three gratings. Additionally the fixed interferometer length imposes a velocity limit, over which particles are unable to interact with all gratings within their Talbot time. Figure 8 depicts the source mechanism used in OTIMA. It consists of a glassy carbon wheel, on which a thin layer of molecular powder is brushed by a felt wheel. From this wheel, the particles are desorbed with a tightly focused laser pulse. The resulting molecular cloud entrained in a supersonically expanding carrier gas pulse to create a molecular beam headed for the interferometer.
The carrier gas pulse is produced using an Even-Lavie valve [60] with a conical nozzle of 100 μm diameter and 25 μs pulse width.

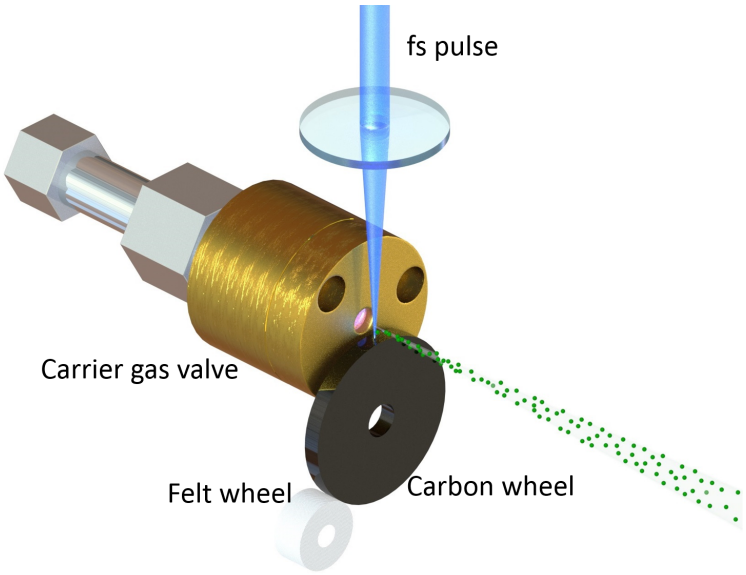

Figure 8: Desorption source: Particles are desorbed from a glassy carbon wheel using a fs-duration laser pulse at 343 nm, focused to a diameter of 100 μm. They are subsequently enveloped by a noble carrier gas undergoing supersonic expansion, produced by an Even Lavie valve. The collisions serve to cool the particles internally and accelerate the to the carrier gas velocity

To create a stable supersonic expansion at a given velocity, one must find a fine balance between several parameters: backing gas pressure, control pulse width as well as choice of carrier gas.
On the other hand, with the right combination of these parameters, it is possible to create molecular beams with nearly free choice of velocity.
The desorption process plays an important role in the source. It operates in the following principle: laser light is focused on a spot on the wheel, ablating coated molecules on its surface. For high enough energy transfer the molecules around the target surface are vaporized. The constituents of the molecular cloud can be traced back to three different processes [61]. The most desirable outcome is the desorption of single molecules into the gas phase. The other possible processes include so-called "phase explosion" and "spallation". In the case of phase explosion the particles are not individually desorbed but ejected from the surface as small droplets that may still break up into individual molecules if they have a high enough stored energy. In the case of spallation, large chunks of the target material are ejected from the surface by laser-induced shock waves.

These chunks are generally too heavy to be carried along by the carrier gas and can be found as visible coating of the source chamber. The physics behind non-resonant laser desorption are complicated and a definitive model is yet to be found. Experimental results [24], also presented in this thesis, give some insight into the possible time scales of the different desorption processes. The laser pulse energy, duration (and also intensity) all influence the fraction of molecules in each state. In [62] it is shown that by reducing the pulse duration for a constant pulse energy, the resulting increase in the laser field strength imparts a much higher temperature to the molecule electrons. The following equilibration transfers more heat to the molecules which then proceed through the melting phase faster. This results in a higher fraction of singly desorbed molecules. The laser currently in use at the OTIMA setup is a *TOPAG "Pharos"* femtosecond laser with a pulse duration of 290 fs. It has a Gaussian beam profile and a beam spot diameter of 3 mm. It can be operated at the base wavelength of 1030 nm with a pulse energy of 220 μJ and a maximum repetition rate of 50 kHz. A second and third harmonic generation unit allows emission at 515 and 343 nm respectively. The recorded measurements were performed using the third harmonic of the laser, with its output energy attenuated from 80 μJ to 35 μJ. The beam is guided to the carbon wheel and focused to 100 μm diameter. The remaining pulse energy on the wheel surface is $\approx$ 15 μJ. In normal operation a repetition rate of 100 Hz is chosen.

3.3 Grating Lasers

The grating lasers must fulfill the following requirements: high photon energy to ensure beam depletion (via ionization or fragmentation), with only single photon absorption ideally, high relative temporal stability with regards to the Talbot time and a coherence length larger than the distance of the molecular beam to the mirror. For this purpose three discharge pumped *GAM "EX50"* excimer lasers with a maximum pulse energy of 4 mJ are used. They have two main emission lines at 157.63 and 157.52 nm [63], with a nominal intensity ratio of 5:1. The lines have a Full Width Half Maximum (FWHM) of 0.85 pm, which gives the lasers a longitudinal coherence length of 2.9 cm. The spectral properties of F_2 lasers are independent of operating conditions such as temperature, gas pressure high voltage level and age of the lasing system. This makes it possible to use three separate fluorine lasers for the gratings. The importance of spectral stability can be described with an example. If a 1 mm region of the standing light waves is used, the wavelength differences between two gratings must be significantly smaller than 3 pm. Otherwise there is a shift of π from one end to the other, canceling out any interference fringes.

After the outcoupler the lasers have a beam profile of 3 × 9 mm^2 with a Flat-top profile in both directions. The lasers have a pulse duration of 8 ns and a jitter below 5 ns. Oxygen has a high absorption cross-section at 157 nm [64] which makes it necessary to evacuate the beam lines and flush them with nitrogen at a pressure of about 1 mbar during operation. To allow attenuation of the laser power a flux of O_2 can be controlled with mass flow controllers. To ensure proper timing, the source lasers and ToF-MS are triggered using three *BNC "Model 575"* pulse generators. Additionally the timing of the interferometer lasers is monitored by GaP-photo diodes and adjusted in a feedback loop by an in-house software package: Molecular Optics Programming System (MOPS)[65]. This program also incorporates the measurement protocol. The grating lasers are operated in two different modes: symmetric (interference) and reference (asymmetric).

3.4 VUV optics

To guide the grating laser beams to the interferometer mirror and produce a standing light wave with minimal loss requires special optics due to most materials being strongly absorptive at λ_L= 157 nm. CaF_2 mirrors offer the highest reflectivity at 96% [66]. Lenses and windows of CaF_2 need a high grade of purity and range between 70 to 95% transmission. The cylindrical lenses focus the laser beams to a spot ≈ 1 cm behind the mirror surface, resulting in a 1 × 10 mm^2 beam profile on the mirror surface. Evacuated beam lines lead to degradation of the optics and contamination by broken hydrocarbons [67]. To counter this, the optics chamber is flooded with nitrogen increasing the background pressure of the chamber from 10^{-3} to 10^{-1} mbar. The most delicate optical component in the experiment is the interferometer mirror. It is a tailor made CaF_2 mirror that has a very small surface roughness. This is needed to keep deformations over the area of a single laser spot to below 5 to 10 nm. For stronger deformations particles in the molecular beam will experience different grating shifts which leads to an averaging of several interference patterns.

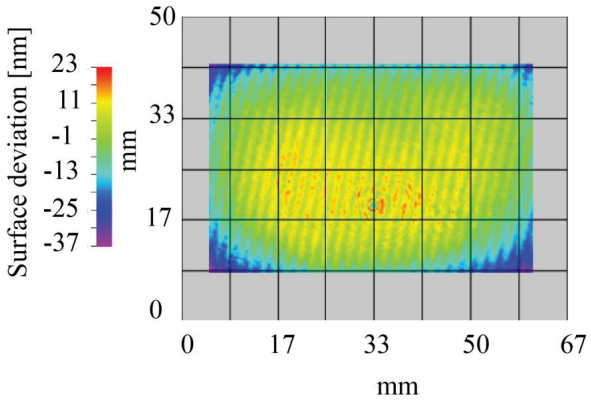

Figure 9: Surface profile of the interferometer mirror currently used in OTIMA. It has a peak-to-peak surface corrugation of 10 nm

The optics still absorb a small fraction of the 157 nm light and subsequently emit blue fluorescence light. This light is caught by a CCD camera and is used to align the gratings by overlapping the spot visible on the interferometer mirror and the bottom window of the main chamber.

3.5 Detection

After passing through the interferometer the particles are ionized in the repeller region of a ToF-MS with a Coherent "Existar EX" laser with has a 2×3 mm^2 beam profile, λ =157.6 nm, $\tau = 7$ ns and up to 2 mJ pulse energy. The reflectron type spectrometer by *Kaesdorf Munich* is orthogonal to the particle beam. Ionized molecules are led through it in two acceleration stages in a Wiley-McLaren mode [68], allowing for a high mass resolution. Afterwards they are detected by a triple stack micro channel plate (MCP) detectors. An analog-to-digital converter (*SP Devices "ADQ412"*) with 1 ns resolution sends the signals to a computer where the ToF-spectra of each measurement mode are collected and averaged. The spectra consist of the measured signal intensity and the flight time t_f for each signal. The ToF-spectra can be converted to mass-spectra in the following way. Each particle receives the same energy by the electric field:

$$mv_\mathrm{f}^2 = c. \tag{40}$$

Since the flight distance is the same for every particle, it is included in c: From this a relation between the flight time and particle mass can be gained:

$$m = \frac{c}{x_{\mathrm{f}}^2} t_{\mathrm{f}}^2 = c' t_{\mathrm{f}}^2. \tag{41}$$

The constant c' can be calibrated to $\Delta m/m = 0.1\%$ using test masses.
The measurement program translates the signal amplitude of the ToF into an accurate estimate of particle counts. This is necessary due to the variance in the signal amplitude caused by different velocities and region of impact on the MCP. To convert to ion counts the program first takes the standard deviation of the background signal for every measurement frame and uses this as a threshold to distinguish between detection and blank events. Detection events are assumed to be caused by single ions to estimate a lower bound. This produces a string of zeros and ones for a single measurement. The number of particles is then calculated by assuming Poissonian statistics for the probability of particle detection $P_{\mathrm{zero}} = \exp(-\lambda)$ with λ the average number of particle counts per frame. The expected number of particles N over M frames is:

$$N = -M \ln(P_{\mathrm{zero}}) \tag{42}$$

The statistical error for S_{int} and S_{ref} is taken to be the standard deviation of $\sqrt{N}$. The 1σ errors for analysis are calculated with Gaussian error propagation.
For a more accurate treatment and errors are determined with Gauss-fits to the recorded mass spectra, taking the area under the fit as a measure of signal intensity.

3.6 Evaluation and Simulation

To determine whether the measured data matches a quantum fringe oscillation or a classical Moiré shadow they must be compared to simulations for both scenarios. To extract information measurement points, a cosine function combined with an enveloping Gaussian function is used t fit the data points

$$S_{\mathrm{F}}(\tau) = V_0 \exp\left[-\left(\frac{\tau^2}{\sigma_{\mathrm{T}}\sqrt{2}}\right)\right] \cos\left(2\pi \frac{\tau - \tau_{\mathrm{off}}}{\sigma}\right). \tag{43}$$

From this fit the overall visibility V_0 can be extracted. To obtain the divergence α the width of the envelope at $1/10$ of the maximum σ_{T} is used.

From the period σ the tilt angle γ can be obtained

$$\alpha = \arcsin\left(\frac{d}{2\sigma_{\mathrm{T}} v_{\mathrm{for}}\sqrt{2\ln(10)}}\right). \tag{44}$$

$$\gamma = \arcsin\left(\frac{d}{\sigma v_{\mathrm{for}}}\right). \tag{45}$$

Together with the expected values of β obtained from quantum chemical computation and measurements of the absorption cross-section, these parameters are fed into the simulations to compare the data points with quantum and classical expectations.
The simulations are based on the theoretical prediction of the signal, seen in equation (32). To obtain valid simulations, several parameters must be fed into the program. The forward velocity of the beam v_{for} in combination with α and γ determine the momentum distribution D and the beam tilt v_γ respectively. The absorbed photons $n_{0,\mathrm{eff}}^{(\mathrm{k})}$ for each grating, combined with β and the chosen separation time $T = kT_{\mathrm{T}}$ determine the signal. For the expected contrast, the chosen value of τ_{ref} is used. The gravitational and static fringe shifts are fed into the parameter b.

4 Results

Performing Gramicidin-interferometry at OTIMA holds many challenges. The grating transmission and separation time, mirror position and molecular beam angle have to be accurately set. However the biggest challenge was the realization of a durable source for Gramicidin. However, using the methods detailed in section 3.2, it has become possible to align for and perform an experiment within a single source refueling cycle, effectively removing the limiting factor of source lifetime. The results presented here are, for the first part, from direct source experiments, comparing fs and ns-desorption efficiency and lifetime for Gramicidin, as well as the successful desorption of massive neutral biopolymers. Also detailed are the interference measurements for Gramicidin in the k = 1 and 1/2 Talbot order as well as the measurements and calculations performed to ensure the quantum nature of measured fringe pattern.

4.1 Femtosecond desorption studies

Switching from nanosecond to femtosecond desorption was motivated by several considerations: in laser ablation studies [62] it had been shown, that edge deformations due to thermal processes around the target are present using ns pulses, but absent in fs illumination. This leads to the assumption that during the laser pulse the absorbing material does not have the time to funnel the energy into its environment. The improved efficiency of femtosecond desorption has already been demonstrated under atmospheric conditions, combining it with electrospray postionization [69].
Here we used an *EKSPLA "NT200 OPO"* emitting at $\lambda_{\mathrm{ns}} = 355$ nm, with a pulse energy $E_{\mathrm{ns}} = 3$ mJ and a pulse duration $\tau_{\mathrm{ns}} = 7$ ns.
For fs desorption a *TOPAG "Carbide"* fs-fiber laser was used. It was operated in two modes: the ultraviolet mode, with $\lambda_{\mathrm{fs}} = 343$ nm, a pulse energy $E_{\mathrm{fs}} = 15$ μJ and a pulse duration $\tau_{\mathrm{fs}} = 293$ fs was used for comparison with ns desorption.
The infrared mode, with $\lambda = 1030$ nm, a pulse energy 15 μJ and a variable pulse duration $\tau = 293$ fs - 10 ps was used to compare the effects of different pulse durations in the ultra short pulse regime.
For the comparison between ns and fs-desorption for the OTIMA source, Gramicidin D (Sigma Aldrich, CAS#) was used, a heterogeneous mixture of different antibiotics. Gramicidin A1, with a mass of 1882 amu, accounts for 80% of the mixture. The experiments were performed at 100 Hz repetition rate. Argon with 30 bar backing pressure was chosen as carrier gas, resulting in a 600 m/s fast molecular beam.

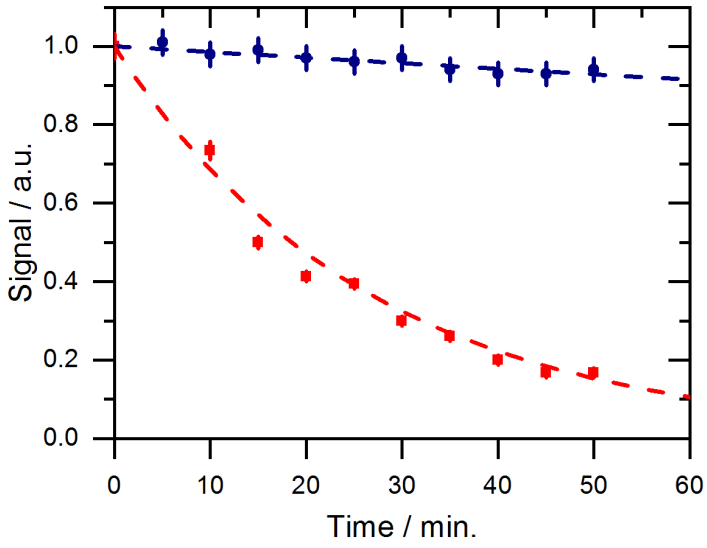

Figure 10: Comparison of Gramicidin signal lifetime for fs and ns-desorption. The colored dashed lines are exponential decay plots to give an estimation of the signal lifetime. While The respective decay constants are $\tau_{\mathrm{fs}} = 676$ min and $\tau_{\mathrm{ns}} = 27$ min. This corresponds to a 25 times longer signal lifetime with fs-desorption. Every data points is averaged over 1000 measurement cycles.

The comparison of signal lifetime was performed by desorbing from a single spot on the carbon wheel and recording mass spectra at 5-minute intervals for both fs and ns lasers. The reduction in signal over time is a good measure of sample consumption. The results are presented in figure 10. While the initial signal strength is comparable for both methods, with ns-desorption the overall signal decreases to $\approx 35\%$ after 30 minutes of operation. Using fs-desorption the signal barely decreases by 5% over the same time. An exponential decay fit to both data sets reveals decay constants of $\tau_{\mathrm{fs}} = 676$ min and $\tau_{\mathrm{ns}} = 27$ min, which translates to over 25 times longer signal lifetime for fs-desorption. A possible reason for this is the much higher yield of individually desorbed molecules from ultra-short-desorption combined with the reduced spreading of hear from the laser pulse reducing the material consumption. The hypothesis for more efficient individual desorption is supported by the much reduced particle coating of the source chamber. Additional measurements with Gramicidin were performed to observe the behavior for varying pulse duration τ_{d} from 300 fs to 10 ps at a stable pulse energy. To freely vary τ_{d}, the laser was operated at λ_{d} =1030 nm. The pulse energy on the carbon wheel was held stable at 15 μJ in a spot of 100 μm diameter. The repetition rate and carrier gas match the previous measurement.

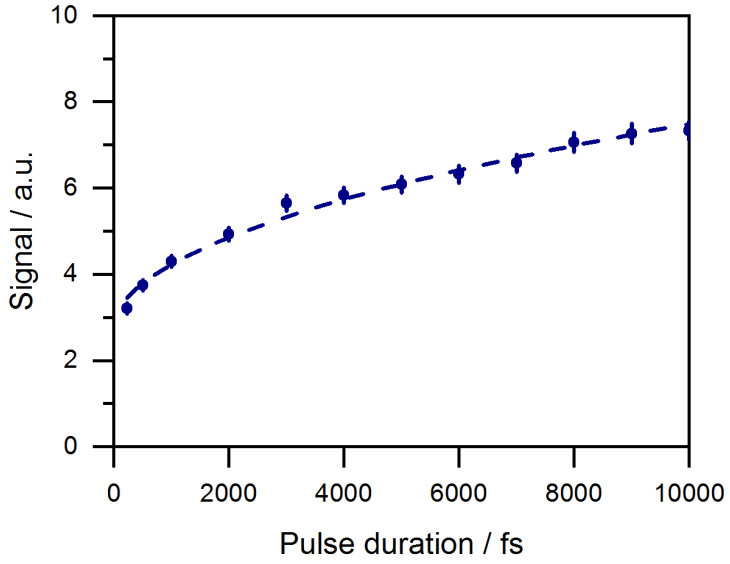

Figure 11: Measured signal intensity as a function of desorption pulse duration. Increasing the duration by a factor of 25 roughly doubles the measured signal intensity. To guide the eye, a square root fit to the data is included. All data points were averaged over 1000 measurement cycles.

From figure 11 it can be seen that increasing the pulse duration increases the signal yield. The increase by a about a factor of 2 for a 25-times longer pulse duration shows that after a certain threshold, the signal gain is weakened. This supports the viewpoint, that at the ps-scale a majority of molecules are desorbed singly into the gas phase. The increased intensity of shorter pulse duration may increase multi-photon processes, leading to a reduced beam signal. This large increase in source-economy even allowed us to produce a neutral biomolecular beam with a mass exceeding 20,000 amu. The particles, seen in figure 2 were tailor-made [24] to test the viability of desorption and photionization in previously unattainable mass regimes. While other commercially available options with similar mass exist, they lack the abundance of Trp needed to be detectable using VUV photoionization.

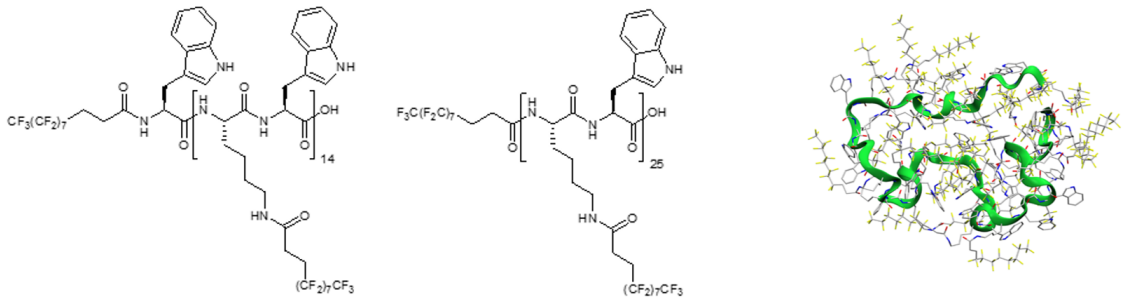

Figure 12: Chemical structure for the compounds used in the desorption experiments. The basic structure is a repeated Lys-Trp combination with fluorinated side chains to improve volatility. The high abundance of Trp-residues in the molecules facilitates VUV ionization, increasing the probability of an absorbed photon. To the right, a folded conformation of compound **2** is shown.

The following results were obtained using Argon at 30 bar backing pressure with the same desorption conditions documented for the test of signal lifetime 10. A first test, using compound **1**, was performed to compare signal intensity and fragmentation behavior of ns and fs-desorption. figure 13 shows the compared mass spectra of fs and ns-desorption. Calibrating the main peak to 11,716 amu leads to a mass separation between the fragment peaks of 788 amu, which matches the mass of a single fluorinated Lys-Trp structure. It is apparent that the different desorption processes influence the overall signal yield, not however the rate of fragmentation. This implies that, should the fragments originate from the source, their fragmentation behavior is not sensitive to the desorption timescale.
An in depth study of the fragmentation behavior would require highly purified samples of the compounds, to exclude masses caused by incomplete synthetization. Desorption and ionization studies of a similar compound [24] show no change in the fragmentation rate of the particles for increased desorption or ionization energy.

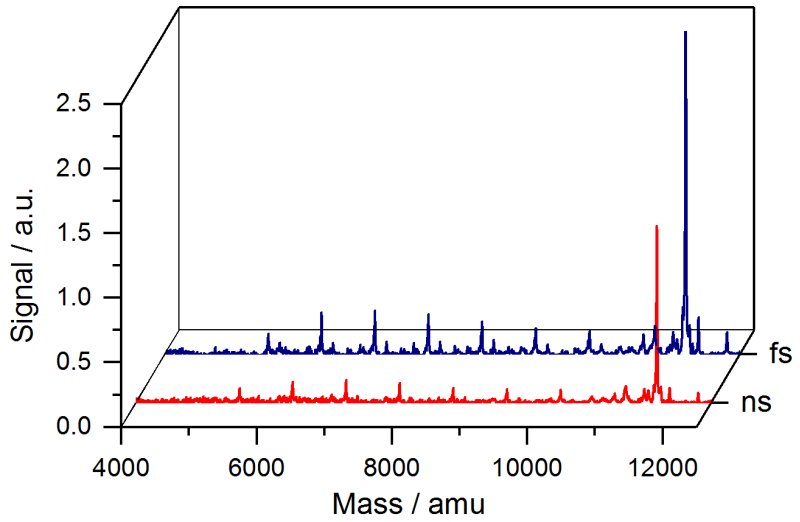

Figure 13: Comparison of mass spectra of compound 1. Both ns and fs spectra were averaged over 5000 frames. The particles were ionized using 157 nm VUV- light. The desorption pulse energy was maintained at 1 mJ for ns and 15 μJ for fs-desorption respecitively, with the light focused to 100 μm diameter on the carbon wheel.

Figure 14 shows the successful desorption of compound **2**. They were desorbed using fs-laser illumination exclusively While the overall highest mass peak is weak compared to the peak of compound **1**, this could be due to insufficient deflection of the ToF-MS, leading to an unresolved mass peak. Additionally, the detection efficiency of the MCPs depends on the velocity of the detected ions. Since all particles in the TOF receive the same energy, this results in slower velocities for heavier particles.
In this case as well, the fragment peaks can be matched to the loss of a fluorinated Trp-Lys group.

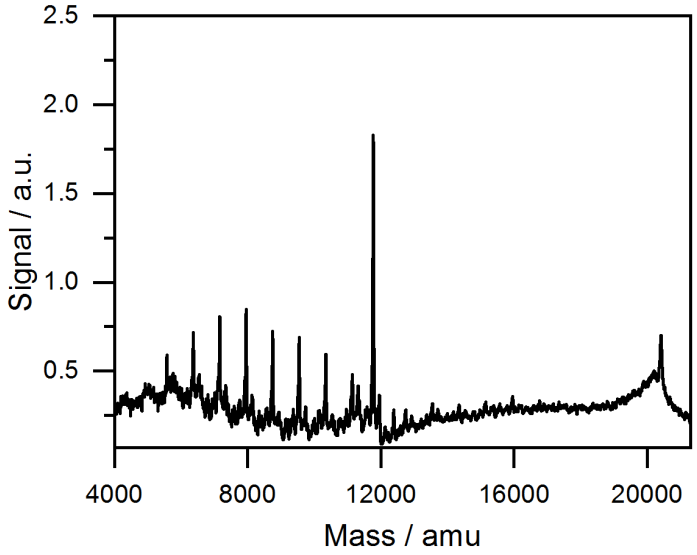

Figure 14: Mass spectrum of a prepared mixture of compound 1 and 2, prepared in a mass ratio of 15:140. The signal of compound 2 stands out clearly above the background noise of the mass spectrum, proving the possibility of launch and postionization for such massive polypeptides. The fragment peaks can be assigned to the loss single of fluoroalkylated Trp-Lys groups. The particles were desorbed using 15 μJ fs-light at 343 nm.

4.2 Gramicidin interference

Performing interference experiments with the antibiotic Gramicidin has been an outstanding challenge at OTIMA. Dip measurements to discriminate between classical shadow and quantum fringe modulation require 5 to 10 minutes for each data point. This leads to a required signal lifetime of just below 2 hours for a typical time-domain resonance dip curve of 11 different timings, not factoring in the required alignment of the interferometer. Dip measurements were performed in the $k = 1$ and $1/2$ Talbot order. The horizontal collimation was set to 0.6 mm to ensure the molecular beam has less width than the light gratings. Vertical collimation was chosen to be 0.6 mm for the $k = 1$ Talbot order. For $k = 1/2$ it was set to 1 mm.
The velocity requirements for the measurements were met by using Argon and Helium as carrier gas, resulting in observed velocities $v_1 = 600$ m/s and $v_{1/2} = 1200$ m/s. The data was post-selected for a maximum jitter of $\Delta\tau \pm 2$ ns. The adverse effects of jitter become noticeable at $\pm$ 6 ns.
Contrast and errors were determined with Gauss-fits to the recorded mass spectra, taking the area under the fit as a measure of signal intensity.

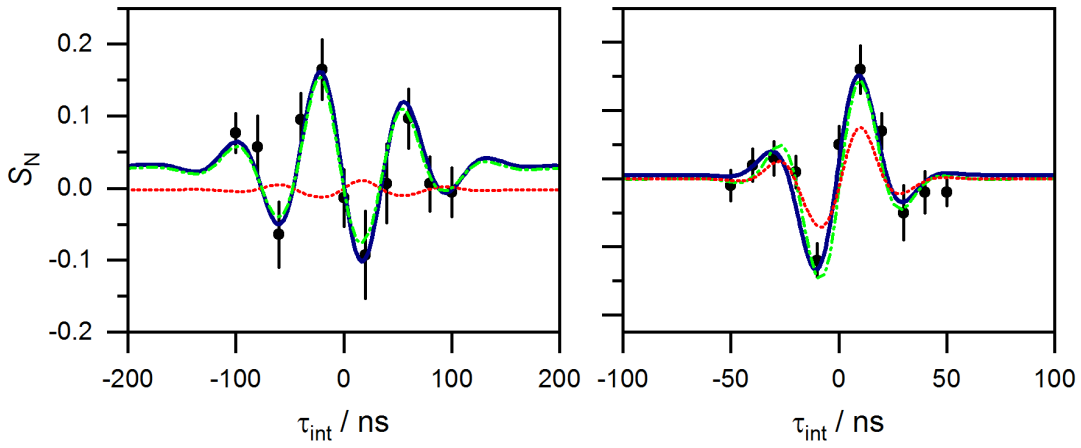

Figure 15: Time-domain resonance dip curves taken with Gramicidin at the $k = 1$ and $1/2$ Talbot order. The quantum simulation (green dashed line) shows a good match to the experimental fit (blue) while the classical simulation (red dots) fails to explain the high contrast data points. All simulations where performed assuming a β value of 0.66 and an average of 2.9 coherently absorbed photons $n_{0,\text{eff}}$ in each grating. The extracted tilt and divergence for both tilts was were fed into the simulations.

As can be seen in figure 15, both interference dips can be clearly distinguished from classical behavior. While the green dashed line, denoting the quantum expectation, is a near perfect match to the experimental fit (blue), the classical expectation (red dotted line) fails to explain many of the data points. The simulations have several parameters which have a major influence on their shape: number of absorbed photons n_0, fringe shift due to mirror deformations b and the factor β described in eq (28). Previous results using the current interferometer mirror [46, 58] have given a good measure of the value of b of around 10 nm. The two other parameters play the largest role in making the distinction between quantum and classical behavior. Due to this it is important to obtain accurate approximations for them. To determine β a series of quantum chemical calculations using *Qchem* [70] were performed in order to obtain the polarizability of Gramicidin at 157.6 nm. These results were combined with a measurement of the ionization cross-section of Gramicidin, as seen in figure 16 to obtain a lower bound for β of 0.64. The measurement to determine the cross-section of gram D at 157 nm was performed by varying the N_2 supply to the ionization beam path, causing a reduction in laser power.
The pulse energy of the laser was measured directly behind an out-coupling window, using a broadband coated pyroelectric power sensor from *thorlabs*. The immediate area around the detector was flushed with N_2 to prevent an erroneously reduced energy measurement. To account for the energy loss due to absorption by the CaF-windows a further set of measurements was performed to compare pulse energy with and without windows, leading to a loss factor of $\approx 20\%$ per window, in good agreement with previous loss measurements [57, 66] of CaF-optics.

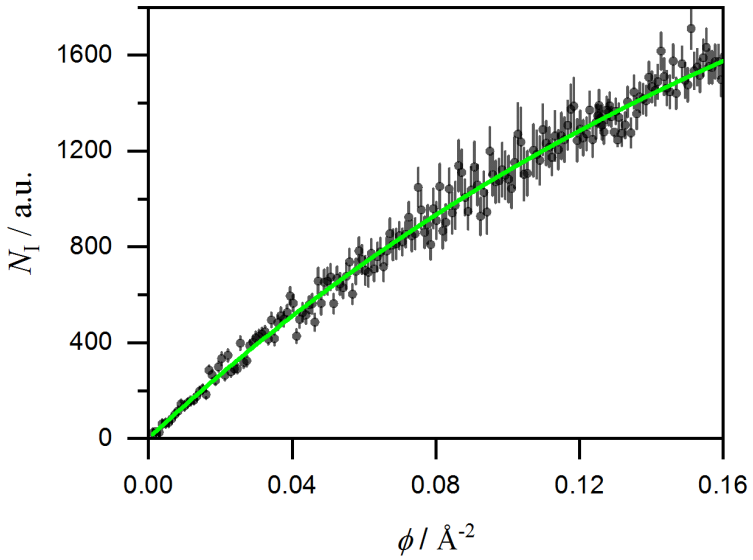

Figure 16: Measurement of the detected signal intensity as a function of the photoionization fluence. The ionization cross-section is extracted using the exponential fit presented in eq. (39), giving a value of $\sigma_\lambda = (4.65 \pm 0{,}21)$ Å^2.

This is far below the value of 80 needed to approximately match the data points with a classical shadow. While the lower bound does not rule out such a high β completely, it can be ruled out with one assumption.
While the ionization cross-section is only a part of the overall absorption cross-section, the OTIMA experiment is only sensitive to beam-depleting relaxation channels, of which ionization is a large fraction. Thus, even assuming heavy fragmentation the required β of 80 is still out of reach. It is important to note here that while several combinations of β and n exist that allow the quantum simulation to match the data points, the classical case always requires an unreasonably large values of β, often exceeding 100, in order to show good agreement with the data.

5 Conclusion and Outlook

This thesis has built on previous work presenting Gramicidin interference [71]. Additional measurements and quantum chemical computations to allow for a clear discrimination between quantum interference and a classical Moiré shadow. Additionally, the many known corrections to the theoretical formalism [46, 71] of OTIMA, accounting for gravity, tilt and divergence of the molecular beam and the corrections for imperfect optics, have now been incorporated into one system to allow accurate predictions for many different molecules, especially at multiples of T_{T} at which the experiment is insensitive to particle internal properties.

5.1 Recoil spectroscopy

The successful interference measurements with Gramicidin pave the way for probing the internal properties of fragile biomolecules. Being a biologically relevant molecule without observable relaxation channels, it presents a perfect candidate for quantum assisted recoil spectroscopy [72].
The motivations for finding new ways to access optical properties are manifold. From determining the absorptive behavior of a molecular system, its energy scales and internal dynamics can be determined. Spectroscopy is one of the main tools to gain such information. While a wide array of techniques exist that allow gas-phase spectroscopy[73], they are currently limited to small, sturdy molecules. For example, most straightforward way to measure spectra absorption is to sublimate the target molecules in a gas cell and measure attenuation of a laser passing through. This can be combined with additional treatment of the molecular cloud to acquire fundamental information about the studied system. Quantum state resolved spectroscopy is one such example, probing a cold molecular cloud to resolve the individual quantum states of the molecule[74].
Such direct studies of gas phase absorption spectra require a well known molecule density that is sufficient to perceptibly attenuate the probing laser intensity. That is only possible if the molecules survive the sublimation process. If that is not the case, different methods sensitive to secondary processes such a dissociation and fluorescence and be used to obtain information about the internal dynamics of the system. If one however wishes to directly probe the absorption behavior of fragile molecules, other methods are required. One such method is quantum assisted recoil spectroscopy. If a particle absorbs a photon it experiences a kick of momentum p_{R} dependent on its wave-number k_{R}: $p_{\mathrm{R}} = \hbar k_{\mathrm{R}}$. The change in particle path corresponding to such an absorption event is not detectable in classical setups.

The high sensitivity of interferometers to small disturbances offers a way to detect such events. By introducing a controllable disturbance, such as a recoil photon, one can measure its effects on the molecule. This is independent of most secondary processes. The principle of the recoil spectroscopy scheme is presented in figure 16.

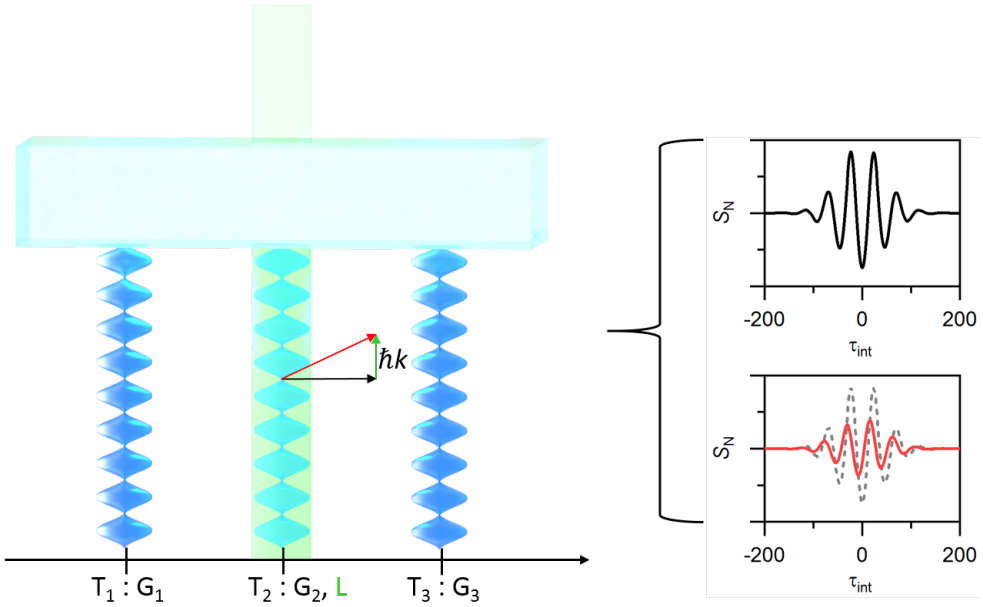

Figure 17: Principle behind the recoil spectroscopy scheme. At the spatio-temporal position of the second grating a tunable recoil laser is introduced to interact with the molecular beam. Absorbing molecules experience a phase shift along the grating vector. This leads to an overall reduction in contrast (red) which can then be compared to a normal contrast measurement (black) to obtain R.

Depending on the absorption cross-section σ at that wavelength λ_R a single particle absorbs n_R photons:

$$n_\mathrm{R} = \frac{\sigma E_\mathrm{R} \lambda_\mathrm{R}}{hcA_\mathrm{R}} \tag{46}$$

This then results in the following reduction R of the visibility:

$$R = \exp\left(-n_\mathrm{L}\left[1 - \cos\left(\frac{2\pi kd}{\lambda_\mathrm{L}}\right)\right]\right) \tag{47}$$

Recoil measurements have already seen successful application at the KDTLI to measure the absorption cross-section of the C_{70} fullerene at 532 nm [75].

There are several advantages to translating this procedure to the OTIMA setup. The time-domain nature of the experiment allows pulsed spectroscopy lasers to be used. Tabletop OPO systems [76] are a ready candidate for such lasers with tunable wavelengths ranging from 215 nm to 1760 nm. CW tabletop counterparts lack the intensity required for a measurable contrast reduction. Furthermore the easy optical access to the interferometer region gives free choice of the spectroscopy laser path. Additionally, the time-domain nature of the experiment allows for an accurate prediction of the expected shift at every wavelength. These advantages combined make the OTIMA setup an attractive candidate for quantum enhanced recoil spectroscopy. Some additional factors must be accounted for however. If the photon absorption causes fluorescence the observed contrast is reduced further. This is caused by the isotropic In conclusion, the future of OTIMA still holds many opportunities for new studies, be it further improvements to pulsed sources or novel spectroscopy techniques to obtain previously unobtainable information about the molecules that shape our everyday life.

5.2 Insulin interference

With the improved source efficiency allowing creation of molecular beams for peptides as massive as compound **2**, interference experiments with heavier biomolecules are a logical goal. Insulin is a viable option for such experiments. While it incorporates a comparable number of amino acids, at 5,807 amu it is much lighter than compound **2**. This makes it a viable option for the current mirror geometry at OTIMA. With roughly three times the Talbot time of Gramicidin, the half order dips recorded here may show to take for Insulin interference.
As a molecule vital to our bodies, Insulin is also an attractive candidate for recoil spectroscopy.

5.3 Further source advances

The improvements to source efficiency and intensity, achieved by use of fs-desorption, are a first step towards the long lived high intensity beams required for future, high mass interference experiments. However, additional steps toward even higher efficiency have to be taken. One possible approach going forward is the use of a liquid capillary fueling mechanism, allowing for precise concentration and flow control of the sample molecules.

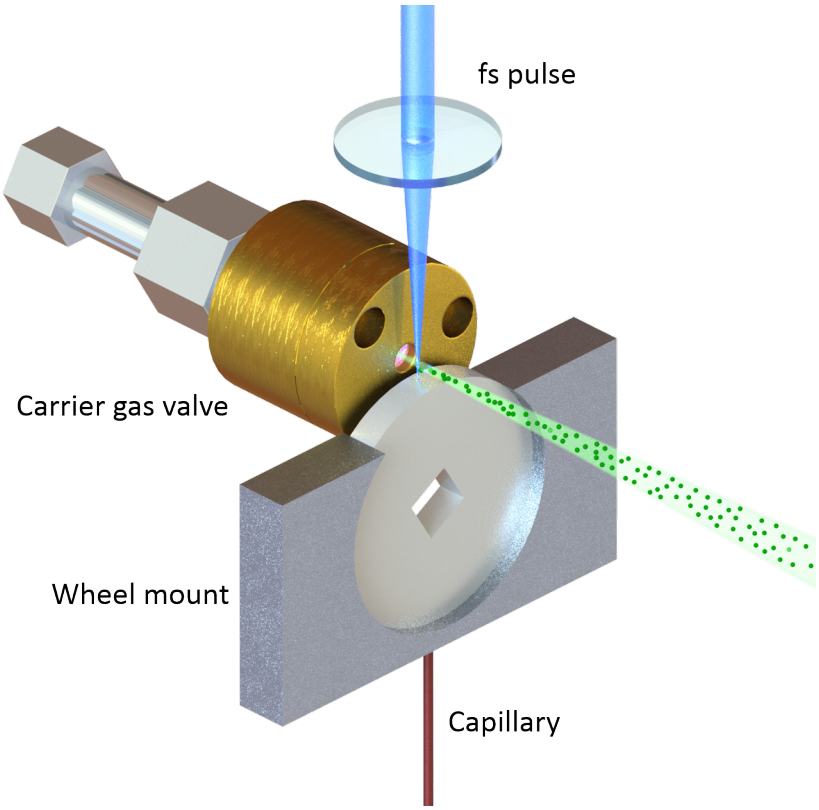

Figure 18: Adapted desorption source for in-vacuo refueling using a capillary. The capillary is connected to an outside reservoir of dissolved molecules. The solution is carried into the vacuum chamber towards a rotating wheel. With sufficient sealing between the wheel and the capillary, the wheel is coated by a dried film of molecules without compromising the vacuum.

Preliminary testing of such a source, seen in figure 18, revealed a very long lived signal using only minute amounts of material when compared to current conditions. However, the instability of the signal, combined with a very high working pressure exceeding 3×10^{-4} mbar, prevent application in its current form. The perfected capillary fueling mechanism could represent a second component needed for meaningful interference experiments with biomolecules of masses exceeding 20,000 amu.

Acknowledgements

It was during the second year of my Bachelor-studies that I first made contact with Markus Arndt and his group. On a whim I asked for an internship position over the summer and, to my surprise, he agreed to take me. This was my first experience of actual laboratories, and I was hooked. The following year I returned to work on my Bachelor thesis and the year after that I began the journey that would be my master thesis, where I turned from an occasional visitor into a member of the group.
With this I want to thank you Markus, for giving me that first opportunity and showing me the amazing world of molecular quantum optics. Thank you for your encouragement and support during this time. I also want to thank Armin Shayeghi, for taking me under your wing at a time where I lost sight of my wonder for science and reigniting that flame. Your tenacity and good humor in the face of setbacks and obstacles are an inspiration to me, as is your boundless curiosity. You kept me going through the hard times in the lab and made the good all the more enjoyable. My thanks go out to the other denizens of room 3K35, for keeping the mood optimistic and friendly throughout the ups and downs of the experiments. I want to thank Philipp Geyer for his invaluable assistance the many times something broke, his diplomacy with the workshop staff and the many interesting if incredulous lunch conversations. I also want to thank everyone frequenting the quantum kitchen for keeping it a place where you can talk about life, the universe and everything.
Finally, I want to thank my family for their support, understanding and the incredible food. You all gave me a place of peace an quiet and the energy to return to the lab each day.

References

[1] Albert Einstein. On a Heuristic Viewpoint Concerning the Production and Transformation of Light. *Ann. Phys.*, 17(6):132–148, 1905.

[2] Albert Einstein. A Brief Outline of the Development of the Theory of Relativity. *Nature*, 106:782–784, 1921.

[3] Louis de Broglie. Waves and quanta. *Nature*, 112:540, 1923.

[4] E Schrödinger. An Undulatory Theory of the Mech of Atoms and Molecules. *Phys. Rev.*, 28(6):1049–1070, 1926.

[5] C. Davisson and L. H. Germer. Davisson Germer. *Phys. Rev.*, 30(6):705–740, 1927.

[6] George Paget Thomson. The Diffraction of Cathode Rays by Thin Films of Platinum. *Nature*, 120:802, 1927.

[7] I Estermann and O Stern. Diffraction of molecular beams. *Zeitschrift für Phys.*, 61(1-2):95–125, 1930.

[8] P. N. Mitchell, D. P., & Powers. Bragg Reflection of Neutrons. *Phys. Rev.*, 50:486–487, 1936.

[9] Sandra Eibenberger, Stefan Gerlich, Markus Arndt, Marcel Mayor, and Jens Tüxen. Matter–wave interference of particles selected from a molecular library exceeding 10000 amu. *Phys. Chem. Chem. Phys.*, 15(35):14696, 2013.

[10] A. Ariga, A. Ereditato, R. Ferragut, M. Giammarchi, M. Leone, C. Pistillo, S. Sala, and P. Scampoli. First observation of antimatter wave interference. *arXiv:1808.08901*, 2018.

[11] H. J. Kimble, M. Dagenais, and L. Mandel. Photon antibunching in resonance fluorescence. *Physical Review Letters*, 39(11):691–695, sep 1977.

[12] J. S. Bell. On the einstein podolsky rosen paradox. *Physics Physique Fizika*, 1(3):195–200, 1964.

[13] Stuart J. Freedman and John F. Clauser. Experimental test of local hidden-variable theories. *Phys. Rev. Lett.*, 28(14):938–941, 1972.

[14] Jian-Wei Pan, Dik Bouwmeester, Matthew Daniell, Harald Weinfurter, and Anton Zeilinger. Experimental test of quantum nonlocality in three-photon Greenberger–Horne–Zeilinger entanglement. *Nature*, 403(6769):515–519, 2000.

[15] Igor Pikovski, Magdalena Zych, Fabio Costa, and Časlav Brukner. Universal decoherence due to gravitational time dilation. *Nat. Phys.*, 11(8):668–672, 2015.

[16] G. C. Ghirardi, A. Rimini, and T. Weber. Unified dynamics for microscopic and macroscopic systems. *Phys. Rev. D*, 34:470–491, 1986.

[17] Roger Penrose. On Gravity's Role in Quantum State Reduction. *Gen. Relativ. Gravit.*, 28(5):581–600, 1996.

[18] M. F. Jarrold. Peptides and proteins in the vapor phase. *Annu. Rev. Phys. Chem.*, 51(1):179–207, 2000.

[19] † Rodolphe Antoine Joly Laure † Abdul-Rahman Allouche † Michel Broyer † Jérôme Lemoine ‡, Philippe Dugourd*†, Laure Joly, Rodolphe Antoine, Abdul Rahman Allouche, Michel Broyer, Jérôme Lemoine, Philippe Dugourd, † Rodolphe Antoine Joly Laure † Abdul-Rahman Allouche † Michel Broyer † Jérôme Lemoine ‡, and Philippe Dugourd*†. Ultraviolet spectroscopy of peptide and protein polyanions in vacuo: Signature of the ionization state of tyrosine. *J. Am. Chem. Soc.*, 129(27):8428–8429, 2007.

[20] Jennifer S. Brodbelt. Photodissociation mass spectrometry: new tools for characterization of biological molecules. *Chem. Soc. Rev.*, 43(8):2757–2783, 2014.

[21] Rodolphe Antoine, Isabelle Compagnon, Driss Rayane, Michel Broyer, Philippe Dugourd, Gary Breaux, Frederick C. Hagemeister, David Pippen, Robert R. Hudgins, and Martin F. Jarrold. Electric susceptibility of unsolvated glycine-based peptides. *J. Am. Chem. Soc.*, 124(23):6737–6741, 2002.

[22] Lukas Mairhofer, Sandra Eibenberger, Joseph P. Cotter, Marion Romirer, Armin Shayeghi, and Markus Arndt. Quantum-Assisted Metrology of Neutral Vitamins in the Gas Phase. *Angew. Chemie - Int. Ed.*, 56(36):10947–10951, 2017.

[23] Rodolphe Antoine, Isabelle Compagnon, Driss Rayane, Michel Broyer, Philippe Dugourd, Nicolas Sommerer, Michel Rossignol, David Pippen, Frederick C. Hagemeister, and Martin F. Jarrold. Application of Molecular Beam Deflection Time-of-Flight Mass Spectrometry to Peptide Analysis. *Anal. Chem.*, 75(20):5512–5516, 2003.

[24] Jonas Schätti, Philipp Rieser, Ugur Sezer, Georg Richter, Philipp Geyer, Gustavo G. Rondina, Daniel Häussinger, Marcel Mayor, Armin Shayeghi, Valentin Köhler, and Markus Arndt. Pushing the mass limit for intact launch and photoionization of large neutral biopolymers. *Communications Chemistry*, 1(1):93, 2018.

[25] Luke Hanley and Ralf Zimmermann. Light and molecular ions: The emergence of vacuum UV single-photon ionization in MS. *Anal. Chem.*, 81(11):4174–4182, 2009.

[26] R. Weinkauf, P. Aicher, G. Wesley, J. Grotemeyer, and E. W. Schlag. Femtosecond versus Nanosecond Multiphoton Ionization and Dissociation of Large Molecules. *J. Phys. Chem.*, 98(34):8381–8391, 1994.

[27] C H Becker, K J Wu, C. H. Beckercor, K. J. Wufn, C H Becker, K J Wu, C. H. Beckercor, and K. J. Wufn. On the photoionization of large molecules. *J. Am. Soc. Mass Spectrom.*, 6(10):883–888, 1995.

[28] E. W. Schlag and R. D. Levine. Ionization, charge separation, charge recombination, and electron transfer in large systems. *J. Phys. Chem.*, 96(26):10608–10616, 1992.

[29] L. Hanley, P. D. Edirisinghe, W. F. Calaway, I. V. Veryovkin, M. J. Pellin, and J. F. Moore. 7.87eV postionization of peptides containing tryptophan or derivatized with fluorescein. *Appl. Surf. Sci.*, 252(19):6723–6726, 2006.

[30] E. W. Schlag, J. Grotemeyer, and R. D. Levine. Do large molecules ionize? *Chem. Phys. Lett.*, 190(6):521–527, 1992.

[31] Optical Society of America. *Handbook of Optics*. Number 2. 2004.

[32] H.F. Talbot. LXXVI. Facts relating to optical science. No. IV. *Philos. Mag. Ser. 3*, 9(56):401–407, 1836.

[33] E Lau. Beugungserscheinungen an Doppelrastern. *Ann. Phys.*, 437(7-8):417–423, 1948.

[34] H. B G Casimir and D. Polder. The influence of retardation on the London-van der Waals forces. *Phys. Rev.*, 73(4):360–372, 1948.

[35] Bj rn Brezger, Markus Arndt, and Anton Zeilinger. Concepts for near-field interferometers with large molecules. *J. Opt. B Quantum Semiclassical Opt.*, 5(2):S82–S89, 2003.

[36] O Nairz, B Brezger, M Arndt, and a Zeilinger. Diffraction of complex molecules by structures made of light. *Phys. Rev. Lett.*, 87(16):160401, 2001.

[37] Ernst M. Rasel, Markus K. Oberthaler, Herman Batelaan, Jörg Schmiedmayer, and Anton Zeilinger. Atom wave interferometry with diffraction gratings of light. *Phys. Rev. Lett.*, 75(14):2633–2637, 1995.

[38] S. Cahn, a. Kumarakrishnan, U. Shim, T. Sleator, P. Berman, and B. Dubetsky. Time-Domain de Broglie Wave Interferometry. *Phys. Rev. Lett.*, 79:784–787, 1997.

[39] P. L. Kapitza and P. A. M. Dirac. The reflection of electrons from standing light waves. *Proc. Camb. Philos. Soc.*, 29:297 – 300, 1933.

[40] Daniel L Freimund and Herman Batelaan. Bragg scattering of free electrons using the Kapitza-Dirac effect. *Phys. Rev. Lett.*, 89(28 Pt 1):283602, 2002.

[41] Ch. J. Bordé, S. Avrillier, A. Van Lerberghe, Ch. Salomon, D. Bassi, and G. Scoles. Observation of optical Ramsey fringes in the 10 μm spectral region using a supersonic beam of SF 6. *Le J. Phys. Colloq.*, 42(C8):C8–15–C8–19, 1981.

[42] Stefan Gerlich, Lucia Hackermüller, Klaus Hornberger, Alexander Stibor, Hendrik Ulbricht, Michael Gring, Fabienne Goldfarb, M. Savas, Marcel Müri, Marcel Mayor, and Markus Arndt. A Kapitza–Dirac–Talbot–Lau interferometer for highly polarizable molecules. *Nat. Phys.*, 3(10):711–715, 2007.

[43] Stefan Nimmrichter, Philipp Haslinger, Klaus Hornberger, and Markus Arndt. Concept of an ionizing time-domain matter-wave interferometer. *New J. Phys.*, 13(7):75002, 2011.

[44] Philipp Haslinger, Nadine Dörre, Philipp Geyer, Jonas Rodewald, Stefan Nimmrichter, and Markus Arndt. A universal matter-wave interferometer with optical ionization gratings in the time domain. *Nat. Phys.*, 9(3):144–148, 2013.

[45] Claudia Keller, Roland Abfalterer, Stefan Bernet, Markus K. Oberthaler, Jörg Schmiedmayer, and Anton Zeilinger. Absorptive masks of light: A useful tool for spatial probing in atom optics. *J. Vac. Sci. Technol. B*, 16(6):3850, 1998.

[46] Nadine Dörre, Jonas Rodewald, Philipp Geyer, Bernd Von Issendorff, Philipp Haslinger, and Markus Arndt. Photofragmentation beam splitters for matter-wave interferometry. *Phys. Rev. Lett.*, 113(23):233001, 2014.

[47] Markus Marksteiner, Alexander Divochiy, Michele Sclafani, Philipp Haslinger, Hendrik Ulbricht, Alexander Korneev, Alexander Semenov, Gregory Gol'tsman, and Markus Arndt. A superconducting NbN detector for neutral nanoparticles. *Nanotechnology*, 20(45):455501, 2009.

[48] Shau Yu Lan, Pei Chen Kuan, Brian Estey, Philipp Haslinger, and Holger Müller. Influence of the coriolis force in atom interferometry. *Phys. Rev. Lett.*, 108(9):90402, 2012.

[49] Nadine Dörre and Markus Arndt. *Time-domain matter-wave interferometry with clusters and large molecules*. PhD thesis, Vienna, 2015.

[50] K Patorski. Incoherent superposition of multiple self-imaging: Lau effect and Moiré fringe explanation. *Opt. Act.*, 30:745–758, 1983.

[51] Björn Brezger, Lucia Hackermüller, Stefan Uttenthaler, Julia Petschinka, Markus Arndt, and Anton Zeilinger. Matter-wave interferometer for large molecules. *Phys. Rev. Lett.*, 88(10):100404, 2002.

[52] Andrey Turlapov, Alexei Tonyushkin, and Tycho Sleator. Talbot-Lau effect for atomic de Broglie waves manipulated with light. *Phys. Rev. A.*, 71(4), 2005.

[53] Stefan Nimmrichter and Klaus Hornberger. Macroscopicity of mechanical quantum superposition states. *Phys. Rev. Lett.*, 110:160403, 2013.

[54] Stefan Nimmrichter. *Macroscopic Matter Wave Interferometry*. Springer, Vienna, 2014.

[55] Stefan Nimmrichter, Klaus Hornberger, Hendrik Ulbricht, and Markus Arndt. Absolute absorption spectroscopy based on molecule interferometry. *Phys. Rev. A*, 78:063607, 2008.

[56] E. Wigner. On the quantum correction for thermodynamic equilibrium. *Phys. Rev.*, 40:749–759, 1932.

[57] Nadine Dörre, Philipp Haslinger, Jonas Rodewald, Philipp Geyer, and Markus Arndt. Refined model for Talbot–Lau matter-wave optics with pulsed photodepletion gratings. *J. Opt. Soc. Am. B*, 32(1):114, 2014.

[58] Jonas Rodewald, Nadine Dörre, Andrea Grimaldi, Phiilipp Geyer, Lukas Felix, Marcel Mayor, Armin Shayeghi, and Markus Arndt. Isotope-selective high-order interferometry with large organic molecules in free fall. *New J. Phys.*, 20:033016, 2018.

[59] Errol G. Lewars. *Computational Chemistry*. Springer Netherlands, 2010.

[60] Uzi Even. The Even-Lavie valve as a source for high intensity supersonic beam. *EPJ Tech. Instrum.*, 2(1):17, 2015.

[61] Richard Knochenmuss. Ion formation mechanisms in UV-MALDI. *Analyst*, 131(9):966, 2006.

[62] X. Liu, D. Du, and G. Mourou. Laser ablation and micromachining with ultrashort laser pulses. *IEEE J. Quantum Electron*, 33(10):1706–1716, 1997.

[63] C J Sansonetti, J Reader, and K Vogler. Precision measurement of wavelengths emitted by a molecular fluorine laser at 157 nm. *Appl. Opt.*, 40(12):1974–8, 2001.

[64] H. Pummer, K. Hohla, M. Diegelmann, and J.P. Reilly. Discharge pumped f2 laser at 1580 a. *Elsevier*, 28(1):104–106, 1979.

[65] Philipp Geyer. *Matter-wave interferometry with complex nanoparticles*. PhD thesis, 2015.

[66] Ch. Görling, U. Leinhos, and K. Mann. Surface and bulk absorption in CaF2 at 193 and 157 nm. *Opt. Commun.*, 249(1-3):319–328, 2005.

[67] K. Boller, R.-P. Haelbich, H. Hogrefe, W. Jark, and C. Kunz. Investigation of carbon contamination of mirror surfaces exposed to synchrotron radiation. *Nuclear Instruments and Methods in Physics Research*, 208(1-3):273–279, 1983.

[68] W. C. Wiley and I. H. McLaren. Time-of-flight mass spectrometer with improved resolution. *Rev. Sci. Instrum.*, 26(12):1150–1157, 1955.

[69] John J Brady, Elizabeth J Judge, and Robert J Levis. Nonresonant femtosecond laser vaporization of aqueous protein preserves folded structure. *Proc. Natl. Acad. Sci. U. S. A.*, 108(30):12217–12222, 2011.

[70] Y. Shao et al. Advances in molecular quantum chemistry contained in the q-chem 4 program package. *Mol. Phys.*, 113:184–215, 2014.

[71] Georg Richter. Time-domain biomolecular interference. Master's thesis, 2018.

[72] Jonas Rodewald, Philipp Haslinger, Nadine Dörre, Benjamin A. Stickler, Armin Shayeghi, Klaus Hornberger, and Markus Arndt. New avenues for matter-wave-enhanced spectroscopy. *Appl. Phys. B Lasers Opt.*, 123(1):1–8, 2017.

[73] Wolfgang Demtröder. *Laserspektroskopie 1.* Springer Berlin Heidelberg, 2011.

[74] P. Bryan Changala, Marissa L. Weichman, Kevin F. Lee, Martin E. Fermann, and Jun Ye. Rovibrational quantum state resolution of the c60 fullerene. *Science*, 363(6422):49–54, 2019.

[75] Sandra Eibenberger, Xiaxi Cheng, Joseph P. Cotter, and Markus Arndt. Absolute absorption cross sections from photon recoil in a matter-wave interferometer. *Phys. Rev. Lett.*, 112(25):250402, 2014.

[76] B Orr, Y He, and R White. Spectroscopic applications of tunable optical parametric oscillators. In *Optical Science and Engineering*, pages 15–95. CRC Press, 2008.

COMMUNICATIONS CHEMISTRY

ARTICLE

https://doi.org/10.1038/s42004-018-0095-y OPEN

Pushing the mass limit for intact launch and photoionization of large neutral biopolymers

Jonas Schätti[1], Philipp Rieser[2], Ugur Sezer[2], Georg Richter[2], Philipp Geyer[2], Gustavo G. Rondina[3], Daniel Häussinger[1], Marcel Mayor[1,4,5], Armin Shayeghi[2], Valentin Köhler[1] & Markus Arndt[2]

Since their first discovery by Louis Dunoyer and Otto Stern, molecular beams have conquered research and technology. However, it has remained an outstanding challenge to isolate and photoionize beams of massive neutral polypeptides. Here we show that femtosecond desorption from a matrix-free sample in high vacuum can produce biomolecular beams at least 25 times more efficiently than nanosecond techniques. While it has also been difficult to photoionize large biomolecules, we find that tailored structures with an abundant exposure of tryptophan residues at their surface can be ionized by vacuum ultraviolet light. The combination of these desorption and ionization techniques allows us to observe molecular beams of neutral polypeptides with a mass exceeding 20,000 amu. They are composed of 50 amino acids – 25 tryptophan and 25 lysine residues – and 26 fluorinated alkyl chains. The tools presented here offer a basis for the preparation, control and detection of polypeptide beams.

[1] Department of Chemistry, University of Basel, 4056 Basel, Switzerland. [2] Faculty of Physics, University of Vienna, Boltzmanngasse 5, 1090 Vienna, Austria. [3] Eduard-Zintl-Institut für Anorganische und Physikalische Chemie, Technische Universität Darmstadt, 64287 Darmstadt, Germany. [4] Institute of Nanotechnology, Karlsruhe Institute of Technology, Hermann-von-Helmholtz-Platz 1, 76344 Eggenstein-Leopoldshafen, Germany. [5] Lehn Institute of Functional Materials (LIFM), Sun Yat-Sen University (SYSU), XinGangXi Road 135, 510275 Guangzhou, P.R. China. [6] Faculty of Physics, University of Vienna, Boltzmanngasse 5, A-1090 Vienna, Austria. Correspondence and requests for materials should be addressed to V.Köh. (email: valentin.koehler@unibas.ch) or to M.A. (email: markus.arndt@univie.ac.at)

Molecular beam science was started at the beginning of the last century[1] to explore the foundations of physics in early tests of the kinetic theory of gases and in the first matter–wave diffraction of atoms and diatomic molecules[2]. Since then, free molecular beams have found diverse applications ranging from atomic clocks[3] and high-resolution molecular spectroscopy[4], over cluster deposition[5] to nanoparticle metrology[6,7] and modern tests of fundamental quantum optics[8–12]. Even functionalized silicon nanocrystals[8] and silver-sulfur nanoparticles[9] have been thermally transferred as neutral particles into high vacuum.

In recent years, unsolvated biomolecules have attracted interest[13–15] since beam experiments allow one to extract intrinsic electronic or structural information of molecules free from any perturbing interactions with a local environment. While charged molecules have been successfully trapped in vacuum for spectroscopy[16], photodissociation[17,18], or photodetachment studies[19], many electronic, magnetic, and optical properties are particularly interesting for neutral particle beams[20]. Beams of isolated molecules[21] were also essential for the analysis of optical[16] and electronic properties of oligopeptides[22] and vitamins[23].

Extending such experiments to large biopolymers and biomimetic particles requires novel methods for transferring them into the gas phase and for detecting them efficiently as well as mass-selectively. While some amino acids[24], nucleotides[25], and functionalized tripeptides[26] can be sublimated or evaporated, large peptides and proteins typically decompose in thermal sources. Nanosecond laser desorption can reduce the heat load and an adiabatically expanding noble gas[27] can cool and carry the molecules toward their subsequent analysis[28]. However, for more than 20 years, it has remained a challenge to desorb and photoionize biopolymers with masses exceeding 2,000 amu[29,30].

Several arguments have been put forward to explain this observation: For instance, internal state relaxation competes with multi-photon ionization[29,31]. This can be reduced using femtosecond ionization[32] but dissipation to non-ionizing states still often dominates in large biopolymers. Single-photon ionization (SPI) can avoid the intermediate levels and close such relaxation channels but it requires typically a photon energy >10 eV, which is beyond the reach of sufficiently intense table-top laser sources[33,34]. Tryptophan (Trp) is the only natural amino acid that can be ionized by a single photon of 7.89 eV as emitted by vacuum ultraviolet (VUV) F_2 lasers.

Gramicidin D and a number of other antibiotic peptides[22] owe their ionization properties to their Trp residues[35]. The role of Trp as an ionizable moiety has been shown for amino acid clusters up to Trp_{30}, which can be abundantly detected using 157.6 nm light[36]. In contrast, photoionization of large covalently bound polypeptides has remained a challenge. A model for the reduced photoionization yield, based on the assumption of rapid electron recapture within the molecule, predicted an exponential decrease with particle mass[31] and negligible efficiency for peptides beyond 2,000 amu, as observed in many experiments so far. We therefore hypothesized that ionization might still be possible if a high number of chromophores could be exposed to vacuum.

Here we show that polypeptides with alternating Trp residues and lysine residues that are amidated with fluoroalkyl chains can be efficiently laser desorbed and postionized. Femtosecond laser desorption enables >25 times higher material economy when compared to nanosecond methods. Polypeptides exceeding 20,000 amu were successfully desorbed and postionized.

Results

Peptide design. Based on these reasonings, we have designed and synthesized five model compounds (see Fig. 1) to build on the antibiotic polypeptide gramicidin D (**1**), which was among the most massive neutral biomolecules in previous beam experiments. Commercial gramicidin D is composed of 15 amino acids, and the most abundant A1 form (molecular weight 1882 amu) contains four Trp residues. Our first tailored model system, decatryptophan Trp_{10} (**2**), contains more than double the number of chromophores at a comparable mass. Since peptide solubility decreases with the number of Trp residues, Trp_{10} represents a practical upper bound to the chain length for a quantitative synthesis of such molecules. The second model compound combines good solubility with high Trp content by alternating Trp with lysine to Ac-$(Lys\text{-}Trp)_5$-OH (**3**). This sequence of alternating amino acids is scalable to long peptides. Compound (**4**) displays the same $(Trp\text{-}Lys)_n$ motif as (**3**) for $n = 10$ and each NH_2 has been amidated with a fluorinated alkyl chain. The total mass therefore exceeds that of gramicidin already by a factor of 4.5. The high fluorine content is intended to reduce intermolecular interactions and to enhance volatility.

In order to maximize the molecular weight at constant Trp ratio, we synthesized the model polymers (**5**) and (**6**) with $n = 14$ and $n = 25$ blocks of $(Lys\text{-}Trp)_n$. They were functionalized in the same way as (**3**). Peptide (**6**) holds 1,960 atoms in 50 amino acid building blocks with a total mass of 20,201 amu. It resembles a protein in macromolecular architecture and mass. The molecules were prepared by standard solid-phase peptide chemistry under Fmoc protection[37]. Fluorinated alkyl groups were introduced by amidation with the respective *N*-hydroxysuccinimide ester after cleavage from the resin[38].

From short-pulse to ultrafast laser desorption of heavy polypeptides. The molecular beam apparatus is sketched in Fig. 2. Analyte powder is picked up by a felt wheel, which transfers a thin layer of molecules onto a counter-rotating glassy carbon wheel. This layer is desorbed by a pulsed focused laser beam[39]. Different desorption lasers were used to answer different questions. Model compounds (**1**)–(**3**) were desorbed by short-pulse infrared laser light (7 ns, 1064 nm, $4–6 \times 10^7$ W cm^{-2}) to explore the role of the Trp content. A quantitative assessment of the importance of the laser pulse duration was realized using gramicidin D (**1**). The high-mass peptides (**4**) and (**5**) show the influence of fluoroalkyl functionalization. They were volatilized using ultraviolet nanosecond pulses (7 ns, 266 nm, $5–8 \times 10^7$ W cm^{-2}). The most massive polypeptide (**6**) was desorbed using *ultrafast*, ultraviolet laser desorption (292 fs, 343 nm) with peak intensities around 5×10^{11} W cm^{-2}.

Once detached from the surface, the analyte molecules are immediately entrained by the atomic carrier gas (argon or neon) that is released by a valve with about 20 µs opening time. The neutral peptides fly 75 cm in high vacuum, across two differentially pumped vacuum chambers. They are then photoionized by a laser pulse at 157 nm to be extracted and detected by orthogonal time-of-flight mass spectrometry.

Influence of the Trp content and fluoroalkyl chains. Figure 3 compares a set of three tailored polypeptides with gramicidin D (**1**), which formed a molecular beam strong enough to saturate the detector after VUV postionization. Assuming that a high Trp content correlates with a high ionization cross-section, we have desorbed decatryptophan (**2**) but find additional fragmentation (For enlarged spectra and peak assignments, see Supplementary Figures 33–38). Substituting half of the Trp residues by lysine units enhances the solubility, facilitates the peptide synthesis and enables soft volatilization with reduced fragmentation, as shown for peptide (**3**). Compound (**4**) is built on this insight and raises the mass by more than a factor of five compared to (**3**), using

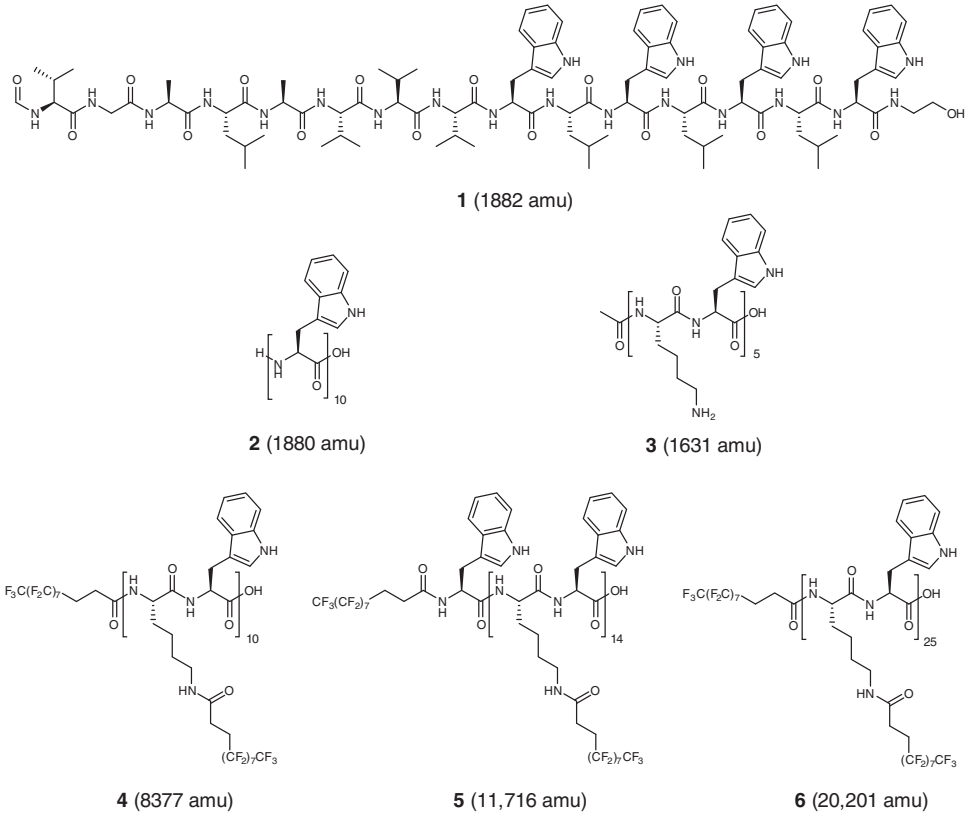

Fig. 1 Iterative design of high mass oligopeptides for molecular beam experiments. Gramicidin A1, as shown here (**1**) is the principal component of commercial gramicidin D. Decatryptophan (**2**) has the highest tryptophan-to-mass ratio of all peptides in our study. Alternating Trp with Lys as in (**3**) provides better solubility and synthetic scalability. The molecular mass and the volatility can be enhanced by capping the NH_2 groups with CO $(CH_2)_2(CF_2)_7CF_3$ groups as in (**4**)-(**6**). (**5**) extends (**4**) to $n = 14$, with a total of 29 amino acids. (**6**) extends (**5**) to $n = 25$, i.e., it contains 50 amino acids. It is functionalized to increase its molecular weight to 20,201 amu and to expose copious amounts of tryptophan to the vacuum

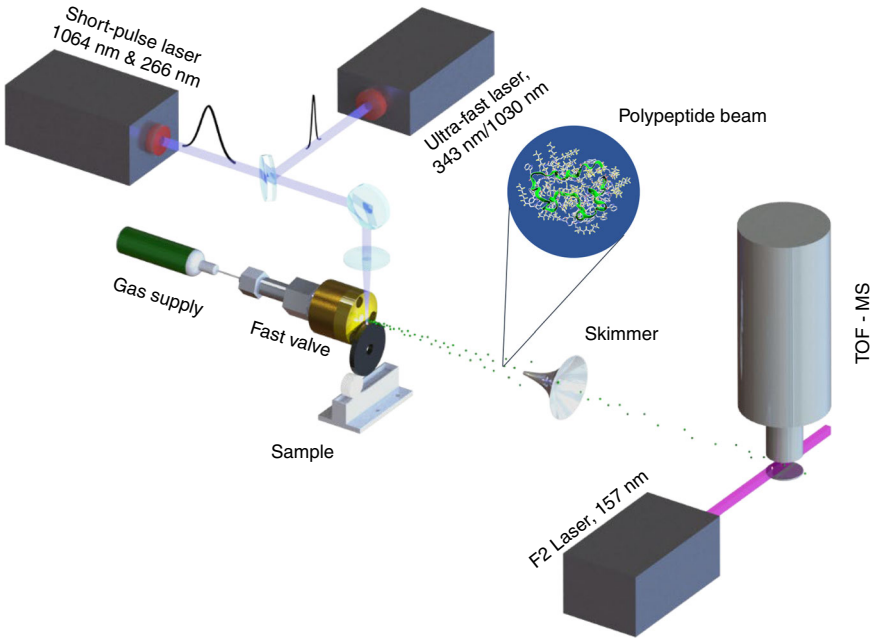

Fig. 2 Molecular beam machine to launch and detect neutral polypeptides. Short or ultrashort laser pulses can be used to desorb the analyte molecules from a powder coated onto a rotating carbon wheel. The individualized polypeptides are entrained by an adiabatically expanding noble gas jet. The molecular beam enters the differentially pumped ionization chamber where a vacuum ultraviolet (VUV) laser pulse (ca. 1 mJ and 10 ns) ionizes it for subsequent analysis by a time-of-flight mass spectrometer (TOF-MS).

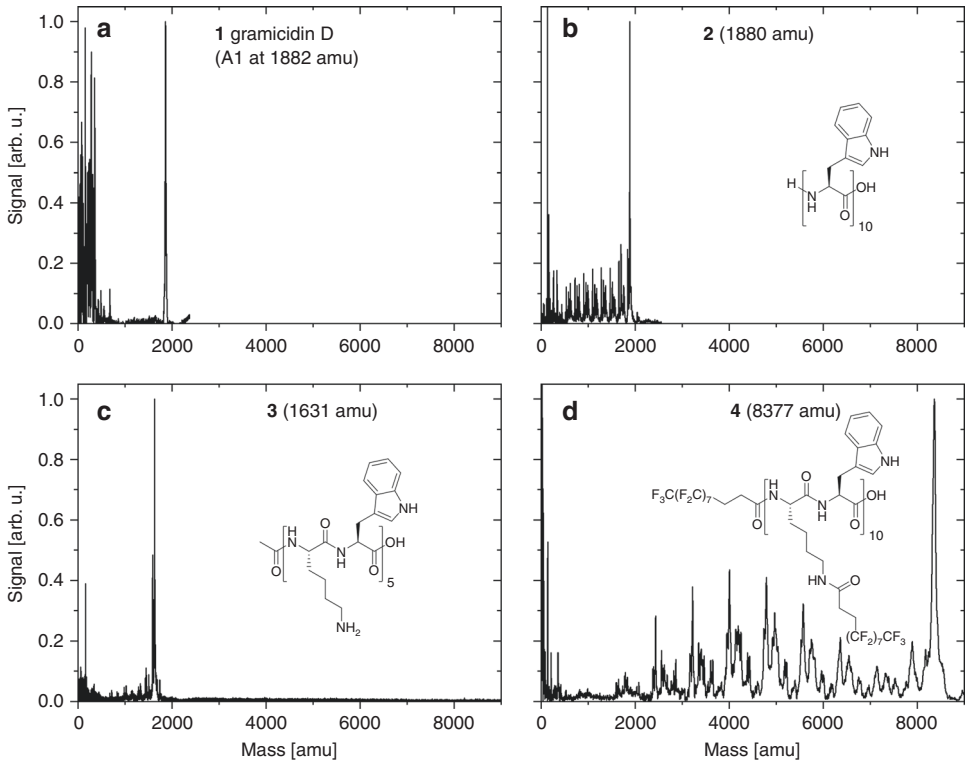

Fig. 3 Nanosecond desorption and VUV ionization of functional polypeptides (**1**)-(**4**). Gramicidin D (**1**) serves as a reference molecule for desorption/postionization experiments. Decatryptophan (**2**) has the highest tryptophan-to-mass ratio and lowest solubility in our series of unmodified peptides. Peptide (**3**) improves on that by substituting every second Trp by Lys. (**4**) is the first step on a new path toward neutral bio-inspired nanoparticle beams and toward a better understanding of the conditions for biopolymer ionization

fluoroalkyl functionalization. Even though peptide (**4**) exhibits more fragments than (**3**), it demonstrates that high-mass peptides can be tailored for neutral molecular beam experiments and be photoionized by VUV laser light.

We have verified the robustness of the mass spectra for various UV nanosecond desorption and ionization energies using compound (**4**) (8377 amu) and oligopeptide (**P7**, Supplementary Figures 41–43, Supplementary Table 2, Supplementary Notes 3–5) (12,320 amu). While we find a threshold behavior followed by saturation for the desorption process (Supplementary Figures 41 and 42 and Supplementary Table 2), the ion yield grows continuously with the ionization energy for the available range of laser pulse energies (Supplementary Figure 43).

On the importance of ultrafast desorption. At a pulse energy of up to 3 mJ, the Q-switched nanosecond laser beam was focused into a spot of 2 mm diameter and reached a peak intensity of about 10^7 W cm^{-2}. This value is comparable to threshold values in matrix-assisted laser desorption ionization (MALDI) experiments[40]. However, several MALDI studies have shown that only a fraction of 10^{-4}–10^{-7} of all desorbed material contributes to the final ion signal[41]. Similarly, in our experiments a substantial fraction of the material is released as nano- and microparticles, which visibly coat the vacuum chamber and are thus lost for the molecular beam.

This indicates an opportunity for substantial improvements and one is led to believe that ultrafast desorption might increase the desorption efficiency, since the absorbed heat will spread less before the pulse energy is transferred and molecules are ejected. This idea has caught on in recent mass spectrometric experiments that combined femtosecond laser desorption with electrospray postionization under atmospheric conditions[42,43]. Here we explore the benefits of ultrafast laser light on biomolecular layers in high vacuum, followed by rapid injection into an adiabatically expanding argon beam. Our ultrafast lasers cover pulse energies up to 80 µJ at 1030 nm and up to 40 µJ at 343 nm with a pulse duration down to 292 fs. We have characterized this idea using gramicidin D (**1**) because of its abundant commercial availability. The robustness of the qualitative form of the mass spectra was first tested for a wide range of desorption conditions, now including femtosecond light (Supplementary Table 2 and Supplementary Figure 40). Comparing then ultrafast desorption at 1030 and 343 nm for comparable pulse durations (292 fs) and energies (15 µJ, on the sample), we find the high UV photon energy (3.6 eV) to be essential for peptide desorption. The energy threshold at this wavelength amounts to about 10 µJ focused in a near-Gaussian waist of ca. 100 µm diameter, i.e., 100 mJ cm^{-2} or 3×10^{11} W cm^{-2} .

Most importantly, the femtosecond pulses improve the sample life time by a factor of >25 in comparison to nanosecond desorption. This is documented in Fig. 4a, where the molecular beam signal is traced as a function of time, while the laser is irradiating the same sample spot with a rate of 100 Hz. The hypothesis that ultrafast desorption favors individualized molecules over the formation of nanoparticles is also corroborated by the fact that the source chamber remains visibly clean.

Figure 4b might suggest that, for the chosen parameters, a laser pulse duration of 10–20 ps already achieves this goal. Reducing the duration by another factor of 33, from 10 ps to 300 fs, the signal decreases by only about a factor of 2. This is consistent with the assumption that most particles depart already as isolated molecules. Reducing the laser pulse length at constant energy and thus increasing the peak intensity may foster multiphoton processes that reduce the molecular beam signal.

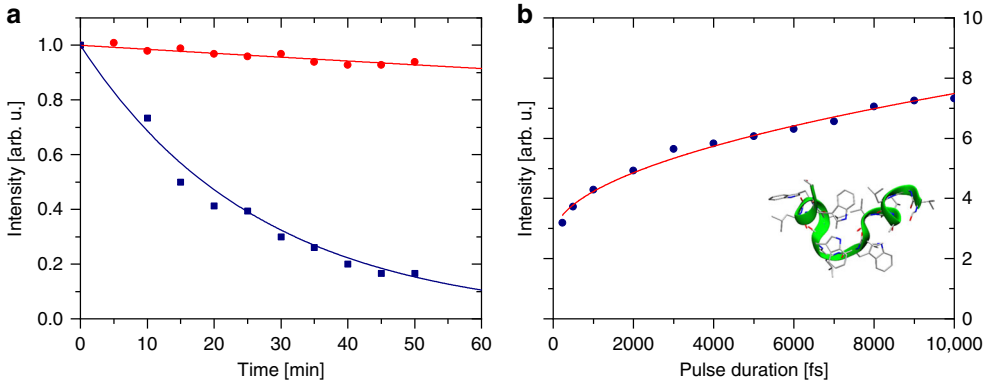

Fig. 4 Molecular beam strength and desorption efficiency as a function of laser pulse duration. **a** Desorption economy: Gramicidin D was desorbed from a thin film. We compare the longevity of a typical sample spot under ultrafast desorption (300 fs at 343 nm, 15 μJ red full circles and line) and short pulse desorption (7 ns at 355 nm, 3 mJ, blue full squares and line). For the same surface area of 100 × 100 μm^2, femtosecond irradiation yields approximately the same initial molecular beam signal but at substantially longer sample life time. The solid lines are exponential fits to the data, with a decay constant of τ_{ns} = 27 and τ_{fs} = 676 min. **b** Desorption laser pulse duration: When varying the pulse duration of infrared light (1030 nm, 40 μJ on 100 × 100 μm^2) irradiating gramicidin D (see inset), we find a smooth increase in the number of detected molecules when the pulse duration is ramped through a factor of 25. The solid line is a square root fit to guide the eye

Improving the material economy by up to two orders of magnitude is a precious advantage in experiments with rare materials, but how would the tremendous laser intensity increase of ultrafast desorption affect the fragmentation pattern? Figure 5 illustrates that ultraviolet desorption can generate a neutral and photoionizable beam of the high-mass peptide (**5**) in both the nanosecond and the femtosecond mode. Comparable integrated signals and fragmentation patterns were obtained; however, at 100 times lower pulse energy, 200 times higher peak intensity and 2 orders of magnitude reduced material consumption in the femtosecond case.

Further exploring the scalability of our new synthesis, desorption, and detection methods, Fig. 6 shows that even the most massive polypeptide in this series can be transferred into a beam of neutral molecules that can be postionized using 157 nm VUV light. This is noteworthy since compound (**6**) is about an order of magnitude more massive than other biopolymers whose photoionization has been reported in the literature so far.

To explore the role of the molecular structure and folding on the exposure of the Trp chromophores to vacuum, canonical-ensemble molecular dynamics simulations were performed for different temperatures. While even at low temperatures a plethora of stretched and coiled structures can stably coexist, we explore the extreme case, starting from the stretched state. While molecule (**6**) can initially extend over >7 nm, our numerical simulations show that it collapses within <100 ps into an energetically more favorable coiled-up tertiary structure upon heating, regardless of the initial state, which is kinetically trapped at low temperature. As a measure of compactness, the average radius of gyration $\langle R_G \rangle$ was calculated as a function of temperature. Figure 7a traces the collapse toward an equilibrium end-to-end distance of about 2 nm beyond $T > 350$ K and $\langle R_G \rangle \simeq$ 1.5 nm. One might worry that the close conformation might bury most chromophores and render photoionization difficult. To obtain an estimate for the exposure of all moieties to vacuum, we have calculated the solvent accessible surface area for the entire molecule as well as for its relevant components, i.e., the Trp and Lys residues as well as the fluoroalkyl chains. Figure 7b shows that the exposed surface area of Trp remains essentially constant over the 0-400 K temperature range and Trp residues are still abundantly exposed to vacuum even in the collapsed state. This can facilitate the escape of electrons after photoionization and distinguishes these Trp-rich polypeptides from many natural proteins (Computational details can be found in the Supplementary Note 2).

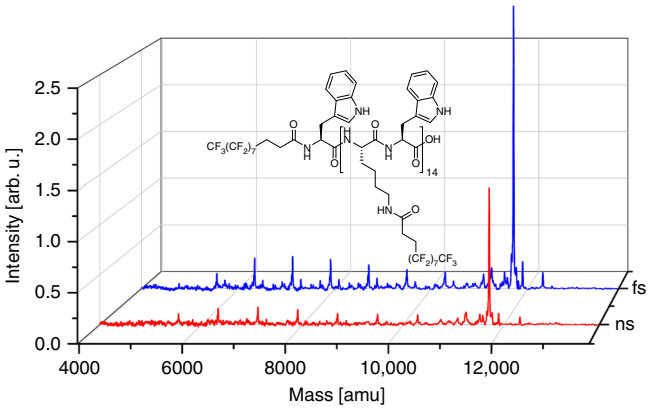

Fig. 5 Mass spectra of the polypeptide (**5**) in comparison between nanosecond and femtosecond desorption. Desorption conditions: short-pulse: $\lambda = 355$ nm, $E = 3$ mJ, $\tau = 7$ ns (red line, foreground). Ultrashort pulse: $\lambda = 343$ nm, $E = 15$ μJ, $\tau = 292$ fs (blue line, background). The different desorption conditions change the desorption efficiency but hardly influence the fragmentation pattern. For peak assignments, see Supplementary Figure 37

Polymer length and desorption/detection efficiency. While earlier papers had speculated that there might be an exponential decrease in the ionization efficiency with increasing mass of the biopolymer, the compounds of our present study were explicitly tailored to avoid this: the number of ionizable Trp chromophores increases in proportion with the polymer length and the simulations show that for all tested circumstances they are arranged abundantly on the molecular surface. While the absorption and ionization probability should thus remain constant with increasing polymer length, the dependence of the volatilization on chain length is less obvious. On the one hand, the equally increasing number of perfluoroalkyl chains reduces the potential stacking of aromatic rings and increase the mass/polarizability or mass/dipole moment ratios. This was already the idea and success of earlier high-mass molecular quantum optics experiments[12]. However, desorbing a given mass and volume of biopolymers

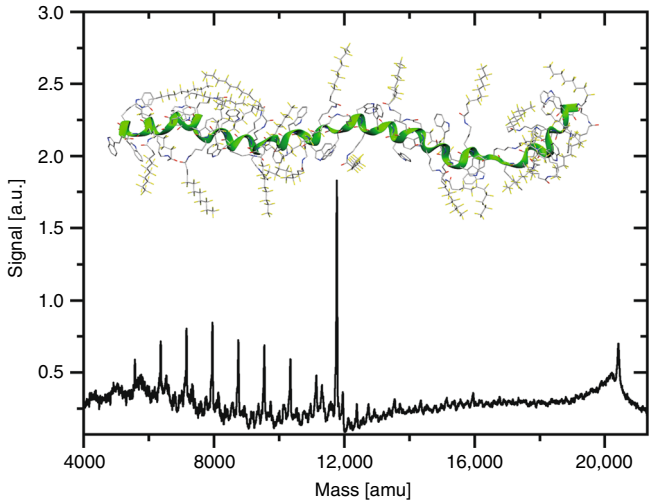

Fig. 6 A neutral molecular beam of massive functionalized polypeptides. A mixture of model peptides (**5**) and (**6**) was prepared in a ratio of 15 mg:140 mg and exposed to ultraviolet femtosecond desorption ($\lambda = 343$ nm, $\tau =$ 292, 15 μJ in 100×100 μm^2). Even compound (**6**) stands out with good signal-to-noise ratio, proving the successful neutral launch and VUV postionization of this massive polypeptide. The fragments are assigned to the cleavage of Trp-Lys(fluoroalkyl) groups (as in Fig. 5) and are also found in the MALDI spectra of the same compounds (Supplementary Figures 24 and 28, see also Supplementary Figures 38 and 39)

must result in 10 times fewer clicks for compound (**6**) at about 20,000 amu compared to gramicidin at not even 2,000 amu. Finally, the secondary electron multiplication efficiency inside the time-of-flight mass spectrometer (TOF-MS) strongly depends on the velocity rather than the kinetic energy of the incident ions. While all molecules are accelerated by the same 16 kV voltage, they reach different velocities, whose influence is critical but not exactly determined for this particular molecular species. This makes it impossible to provide a clear functional dependence. However, we do not observe any substantial decay in signal/noise across the biopolymer mass range of 3,832–12,320 amu.

Discussion

Our study shows that a combined approach of synthetic design and ultrafast desorption enables *the soft launch* of neutral high-mass polypeptides up to the complexity of small proteins into *neutral* molecular beams and their successful soft photoionization. This could be achieved for bio-inspired nanoparticles composed of 50 amino acids and exceeding 20,000 amu, i.e., an order of magnitude higher than seen on native peptides. The functionalized polypeptide (**6**) is 350% more massive and contains 250% more atoms than insulin (51 residues, 5803 amu, 788 atoms).

Exploiting bio-mimetic growth principles, the tailored compounds can be synthesized with atomically defined composition and structure. It seems possible to ligate two or more of these chains to design bio-mimetic molecules with defined mass and atomic sequence to much higher masses, in future.

The peptide design focused on the abundant inclusion of Trp, which is the only natural amino acid compatible with single-photon VUV postionization using table top laser sources at 157 nm. The high Trp abundances also ensures that these chromophores will be exposed to vacuum, even in coiled-up peptides. This has been crucial for the successful in situ mass analysis of the initially neutral molecular beam. For the largest polypeptide in our series, ultrafast ultraviolet desorption was essential. And even for peptides up to 2,000 amu, fs-desorption was >25 times more material efficient than nanosecond methods. Ultrafast desorption therefore promises to also improve on mass spectrometry in combination with novel ionization methods. Intriguing progress on native proteins had been reported using electrospray post-ionization before[43,44].

The high susceptibility of Trp-rich peptides to VUV SPI will also be of importance for advanced macromolecular matter–wave experiments where photo-depletion gratings[45,46] provide novel beam splitters for complex biomolecular matter–waves. Polypeptides exceeding 20,000 amu are therefore interesting candidates for the next generation of matter–wave interference experiments, which can cope with de Broglie wavelengths as small as 50 fm.

Methods

Sample preparation and desorption. A homogeneous distribution of the molecules is established by first dissolving them and loading a felt wheel, which rubs against the counter-rotating glassy carbon wheel[39]. For the nanosecond desorption of compound (**4**), the sample was premixed with Trp in a ratio of 1:20. This procedure was not necessary for the femtosecond experiments. The Vienna TOF-MS was calibrated to the Swiss MALDI TOF results via a linear transformation using all sizeable peaks of the mass distribution of (**5**) and (**6**) up to 20,000 amu.

Four different laser types were compared in the desorption experiments (See Supplementary Table 2 for detailed conditions of every single experiment):

Short-pulse ultraviolet light, emitted by the fourth harmonic of the flash-lamp pumped *Innolas Spitlight 400*: wavelength $\lambda = 266$ nm, duration $\tau_d = 7 \pm 2$ ns.

Short-pulse ultraviolet light, emitted by an *EKSPLA* "*NT200 OPO*" laser: $\lambda =$ 355 nm, $\tau_d = 7 \pm 2$ ns, $E = 1.5$ mJ.

Ultrafast infrared light, emitted by *a TOPAG* "*Carbide*" fs-fiber laser: $\lambda = 1030$ nm, $\tau_d = 292$ fs–10 ps, $E_d < 40$ μJ on the sample

Ultrafast ultraviolet light, *343* nm, *ultrafast* pulse, emitted by a *TOPAG* "*Carbide*" fs-fiber laser: $\lambda = 343$ nm, $E = 40$ μJ.

Supersonic expansion and molecular beam velocity. A noble gas jet is released by an Even–Lavie valve[47] with a backing pressure between 2 and 50 bar and a pulse duration of 20–22 μs. The experiments were performed using argon or neon with a purity of 99.999%. The gas and the polypeptides travel through a differentially pumped vacuum chamber, separated by a 3-mm skimmer, 55 cm behind the source and 20 cm from the ionization region. During operation at 100 Hz, the residual pressure is ca. 5×10^{-5} mbar in the source chamber and 5×10^{-7} mbar or 2×10^{-8} mbar in the detector chamber, for the nanosecond tests on (**1**)–(**4**) and the fs-tests on (**5**) and (**6**), respectively. For gramicidin D (**1**), we observe a mean velocity of 590 m s^{-1} with a full width at half maximum of 80 m s^{-1}. The absence of any major velocity slip and the width of the distribution suggest that the number of collisions suffices to thermalize the translational energy spread of gramicidin to a temperature of 18 K. This is a lower limit to the expected rotational and vibrational temperature of this peptide.

Ion detection. The peptides were ionized by light from a fluorine laser (*Coherent Excistar*) with $\lambda = 157$ nm, $\tau_i = 10$ ns, $E_i = 1$–2 mJ, $A = 3 \times 3$ mm^2 and analyzed using an orthogonal TOF-MS (Kaesdorf München). Model compounds (**1**)–(**4**) were detected using an orthogonal TOF-MS $\Delta m{:}m = 1{:}500$ and baseline corrected. For (**5**)–(**6**), we used an orthogonal reflectron TOF-MS ($\Delta m{:}m = 1{:}500$). Both spectrometers accelerate the ions by 16 kV and count them by electron multiplication using a triple-stack of multi-channel plates. Figure 4: Every point was integrated 5 times over 1000 mass spectra. Figure 6: Each spectrum contained 10^6 points and was smoothed using a running average of 100 points (SI).

Synthetic procedures and characterization of compounds. See Supplementary Methods and Supplementary Note 1, Supplementary Table 1, Supplementary Figures 1–32.

Computational details. See Supplementary Note 2.

Laser desorption/photoionization mass spectra and conditions. See Supplementary Figures 33–39, 40, 42, 43 and Supplementary Notes 3–5, Supplementary Table 2.

Influence of the desorption laser wavelength and pulse length on the character of the mass spectrum. See Supplementary Note 3 and Supplementary Figure 40.

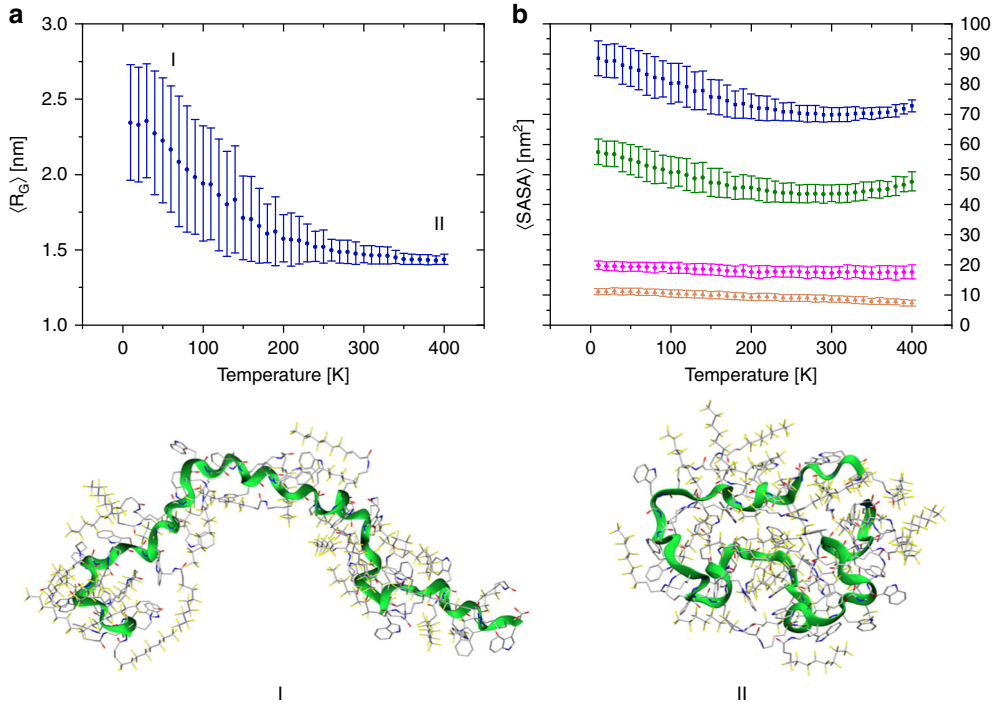

Fig. 7 Structural parameters obtained with canonical-ensemble molecular dynamics simulations. **a** Temperature dependence of the radius of gyration $\langle R_G \rangle$ of polypeptide (**6**). Even when starting from a stretched state, the molecule rapidly coils into a closed tertiary structure with increasing temperature. **b** The average solvent accessible surface area ⟨SASA⟩ quantifies the exposure of different parts of the molecule, here to vacuum. The total area (blue squares) decreases with increasing temperature, as expected but slowly increases beyond 300 K because of the increased exposure of the fluoroalkyl chains (green circles). The tryptophan residues (magenta diamonds) remain almost fully exposed at all temperatures, while the lysine surface (orange triangles) shrinks slightly. Error bars correspond to the standard deviation of the mean.

Influence of the desorption energy/fluence. See Supplementary Note 4 and Supplementary Figure 41.

Influence of the ionization energy/fluence on the normalized mass peak. See Supplementary Note 5 and Supplementary Figures 42 and 43.

Data availability

All relevant data are available from the authors upon reasonable request.

Received: 19 September 2018 Accepted: 16 November 2018
Published online: 10 December 2018

References

1. Stern, O. Zur Methode der Molekularstrahlen. I. *Z. Phys.* **39**, 751–763 (1926).
2. Estermann, I. & Stern, O. Beugung von Molekularstrahlen. *Z. Phys.* **61**, 95–125 (1930).
3. Rabi, I. I., Millman, S., Kusch, P. & Zacharias, J. R. The molecular beam resonance method for measuring nuclear magnetic moments. The magnetic moments of $_3Li^6$, $_3Li^7$and $_9F^{19}$. *Phys. Rev.* **55**, 526–535 (1939).
4. Bordé, C. J. et al. Observation of optical Ramsey fringes in the 10 μm spectral region using a supersonic beam of SF_6. *J. Phys. Coll.* **42**, C8-15–C8-18 (1981).
5. Barth, J. V., Costantini, G. & Kern, K. Engineering atomic and molecular nanostructures at surfaces. *Nature* **437**, 671–679 (2005).
6. de Heer, W. A. The physics of simple metal clusters: experimental aspects and simple models. *Rev. Mod. Phys.* **65**, 611–676 (1993).
7. Schmidt, M., Kusche, R., Issendorff, B. V. & Haberland, H. Irregular variations in the melting point of size-selected atomic clusters. *Nature* **393**, 238–240 (1998).
8. Schöllkopf, W. & Toennies, J. P. Nondestructive mass selection of small Van der Waals clusters. *Science* **266**, 1345–1348 (1994).
9. Chapman, M. S. et al. Optics and interferometry with Na_2 molecules. *Phys. Rev. Lett.* **74**, 4783–4786 (1995).
10. Arndt, M. et al. Wave-particle duality of C60 molecules. *Nature* **401**, 680–682 (1999).
11. Akoury, D. et al. The simplest double slit: interference and entanglement in double photoionization of H2. *Science* **318**, 949–952 (2007).
12. Hornberger, K., Gerlich, S., Haslinger, P., Nimmrichter, S. & Arndt, M. Colloquium: quantum interference of clusters and molecules. *Rev. Mod. Phys.* **84**, 157–173 (2012).
13. Scherman, J.-P. *Spectroscopy and Modelling of Biomolecular Building Blocks* (Elsevier, Amsterdam, 2008).
14. Jarrold, M. F. Peptides and proteins in the vapor phase. *Annu. Rev. Phys. Chem.* **51**, 179–207 (2000).
15. Meyer, T., Gabelica, V., Grubmüller, H. & Orozco, M. Proteins in the gas phase. *Wires Comp. Mol. Sci.* **3**, 408–425 (2013).
16. Laure, J. et al. Ultraviolet spectroscopy of peptide and protein polyanions in vacuo: signature of the ionization state of tyrosine. *J. Am. Chem. Soc.* **129**, 8428–8429 (2007).
17. Viglino, E., Shaffer, C. J. & Turecek, F. UV/Vis action spectroscopy and structures of tyrosine peptide cation radicals in the gas phase. *Angew. Chem. Int. Ed.* **55**, 7469–7473 (2016).
18. Brodbelt, J. S. Photodissociation mass spectrometry: new tools for characterization of biological molecules. *Chem. Soc. Rev.* **43**, 2757–2783 (2014).
19. Gabelica, V. et al. Electron photodetachment dissociation of DNA polyanions in a quadrupole ion trap mass spectrometer. *Anal. Chem.* **78**, 6564–6572 (2006).
20. Antoine, R. et al. Electric susceptibility of unsolvated glycine-based peptides. *J. Am. Chem. Soc.* **124**, 6737–6741 (2002).
21. Grotemeyer, J., Bösel, U., Walter, K. & Schlag, E. W. Biomolecules in the gas phase. 1. Multiphoton-ionization mass spectrometry of native chlorophylls. *J. Am. Chem. Soc.* **108**, 4233–4234 (1986).
22. Antoine, R. et al. Application of molecular beam deflection time-of-flight mass spectrometry to peptide analysis. *Anal. Chem.* **75**, 5512–5516 (2003).
23. Mairhofer, L. et al. Quantum-assisted metrology of neutral vitamins in the gas phase. *Angew. Chem. Int. Ed.* **56**, 10947–10951 (2017).
24. Weinkauf, R., Schermann, J. P., de Vries, M. S. & Kleinermanns, K. Molecular physics of building blocks of life under isolated or defined conditions. *Eur. Phys. J. D* **20**, 309–316 (2002).
25. Gabelica, V. *Nucleic Acids in the Gas Phase* (Springer, Heidelberg, New York, Dordrecht, London, 2014).
26. Schätti, J. et al. Tailoring the volatility and stability of oligopeptides. *J. Mass Spectrom.* **52**, 550–556 (2017).

27. Meijer, G., de Vries, M. S., Hunziker, H. E. & Wendt, H. R. Laser desorption jet-cooling of organic molecules cooling characteristics and detection sensitivity. *Appl. Phys. B* **51**, 395–403 (1990).
28. Grotemeyer, J., Boesl, U., Walter, K. & Schlag, E. W. Biomolecules in the gas phase. II. Multiphoton ionization mass spectrometry of angiotensin I. *OMS Lett.* **21**, 595–597 (1986).
29. Schlag, E., Grotemeyer, J. & Levine, R. Do large molecules ionize? *Chem. Phys. Lett.* **190**, 521–527 (1992).
30. Becker, C. H. & Wu, K. J. On the photoionization of large molecules. *J. Am. Soc. Mass Spectrom.* **6**, 883–888 (1995).
31. Schlag, E. W. & Levine, R. D. Ionization, charge separation, charge recombination, and electron transfer in large systems. *J. Phys. Chem.* **96**, 10608–10616 (1992).
32. Weinkauf, R., Aicher, P., Wesley, G., Grotemeyer, J. & Schlag, E. W. Femtosecond versus nanosecond multiphoton ionization and dissociation of large molecules. *J. Phys. Chem.* **98**, 8381–8391 (1994).
33. Akhmetov, A., Moore, J. F., Gasper, G. L., Koin, P. J. & Hanley, L. Laser desorption postionization for imaging MS of biological material. *J. Mass Spectrom.* **45**, 137–145 (2010).
34. Hanley, L. & Zimmermann, R. Light and molecular ions: the emergence of vacuum UV single-photon ionization in MS. *Anal. Chem.* **81**, 4174–4182 (2009).
35. Hanley, L. et al. 7.87eV postionization of peptides containing tryptophan or derivatized with fluorescein. *Appl. Surf. Sci.* **252**, 6723–6726 (2006).
36. Marksteiner, M. et al. Gas-phase formation of large neutral alkaline-earth metal tryptophan complexes. *J. Am. Soc. Mass Spectrom.* **19**, 1021–1026 (2008).
37. Chan, W. C. & White, P. D. *Fmoc Solid Phase Peptide Synthesis* (Oxford University Press, Oxford, 2000).
38. Malik, L. et al. Perfluoroalkyl chains direct novel self-assembly of insulin. *Langmuir* **28**, 593–603 (2011).
39. Gahlmann, A. P., Sang, T. & Zewail, A. H. Structure of isolated biomolecules by electron diffraction-laser desorption: uracil and guanine. *J. Am. Chem. Soc.* **131**, 2806–2808 (2009).
40. Hillenkamp, F., Karas, M., Beavis, R. C. & Chait, B. T. Matrix-assisted laser desorption/ionization mass spectrometry of biopolymers. *Anal. Chem.* **63**, 1193A–1203A (1991).
41. Knochenmuss, R. & Zenobi, R. MALDI ionization: the role of in-plume processes. *Chem. Rev.* **103**, 441–452 (2003).
42. Brady, J. J., Judge, E. J. & Levis, R. J. Mass spectrometry of intact neutral macromolecules using intense non-resonant femtosecond laser vaporization with electrospray post-ionization. *Rapid Commun. Mass Spectrom.* **23**, 3151–3157 (2009).
43. Brady, J. J., Judge, E. J. & Levis, R. J. Nonresonant femtosecond laser vaporization of aqueous protein preserves folded structure. *Proc. Natl Acad. Sci. USA* **108**, 12217–12222 (2011).
44. Cui, Y. et al. Molecular imaging and depth profiling of biomaterials interfaces by femtosecond laser desorption postionization mass spectrometry. *ACS Appl. Mater. Interfaces* **5**, 9269–9275 (2013).
45. Haslinger, P. et al. A universal matter-wave interferometer with optical ionization gratings in the time domain. *Nat. Phys.* **9**, 144–148 (2013).
46. Dörre, N. et al. Photofragmentation beam splitters for matter-wave interferometry. *Phys. Rev. Lett.* **113**, 233001 (2014).
47. Bahat, D., Cheshnovsky, O., Even, U., Lavie, N. & Magen, Y. Generation and detection of intense cluster beams. *J. Phys. Chem.* **91**, 2460–2462 (1987).

Acknowledgements

This project has received funding from the European Research Council (ERC) under the European Union's Horizon 2020 research and innovation program (Grant Nr. 320694), the Austrian Science Fund (FWF) within program W1210-N25, the Swiss National Science Foundation 200020-178808), and the Swiss Nanoscience Institute (P1403). The computational results were obtained using the Vienna Scientific Cluster (VSC); PRO-BIOTIQUS 70918. A.S. acknowledges funding by the (FWF) within the Lise-Meitner fellowship M 2364. G.G.R. is thankful for funding from the Brazilian National Council for Scientific and Technological Development (206729/2014-6). We gratefully acknowledge the loan of a *Carbide* femtosecond laser by TOPAG Germany and a *Monaco* fs-laser from Coherent Inc. Germany.

Author contributions

The experiments were conceived by M.A., V.K., M.M., U.S. and A.S. The molecular design and synthesis was realized by J.S., V.K. and M.M. The nanosecond experiments were realized by U.S., P.R. and P.G. The femtosecond experiments were realized by P.R., G.R., and A.S. Data analysis was performed by J.S., U.S., G.R., P.R., A.S. and M.A. NMR experiments were carried out and analyzed by J.S. and D.H. Molecular dynamics simulations were designed and analyzed by A.S., G.G.R. and M.A. and realized by G.G. R. The manuscript was written by M.A., V.K. and J.S. with contributions from all authors.

Additional information

Supplementary information accompanies this paper at https://doi.org/10.1038/s42004-018-0095-y.

Competing interests: The authors declare no competing interests.

Reprints and permission information is available online at http://npg.nature.com/reprintsandpermissions/

Publisher's note: Springer Nature remains neutral with regard to jurisdictional claims in published maps and institutional affiliations.